Hamiltonian truncation and quantum simulation of strong-field QED beyond tree level

Patrick Draper,[1,*] Luis Hidalgo,[1,†] and Anton Ilderton[2,‡]
[1]*Department of Physics, University of Illinois, Urbana, Illinois 61801, USA*
[2]*Higgs Centre, School of Physics and Astronomy, University of Edinburgh, EH9 3FD, United Kingdom*

(Received 10 October 2025; accepted 5 February 2026; published 9 March 2026)

Quantum electrodynamics in strong background fields provides an interesting class of problems for classical and quantum simulation. In this paper we formulate simulations of polarization (helicity) flip for a photon colliding with a high-intensity plane wave. Polarization flip is a one-loop effect, which requires addressing new issues that do not arise in simulations of tree-level processes. Working in the momentum-space Fock basis, while convenient for the extraction of scattering amplitudes, requires tuning counterterms to cancel large cutoff effects. We compute analytic formulas for the counterterms at one loop. We then construct circuits for quantum simulations of the process, perform noiseless simulations on classical computers to assess discretization errors, and discuss resource estimates for future simulations on quantum hardware.

DOI: 10.1103/4lmx-psvz

I. INTRODUCTION

Strong electromagnetic fields access processes that are not otherwise easily observed in quantum electrodynamics (QED), including e.g. nonperturbative pair-production [1] and vacuum polarization effects [2–5], as well as a host of classical and quantum nonlinearities which are accessible with current laser technology [6–9]. While many tools have been developed to study "strong-field QED" it remains challenging to account analytically for realistic background fields, higher multiplicity scattering, and higher-loop corrections, see [10,11] for recent reviews.

In light of this it is interesting to explore numerical tools. In the low energy regime of quantum chromodynamics (QCD), lattice Monte Carlo methods provide high precision first-principles access to equilibrium properties and few-particle scattering amplitudes [12]. Unfortunately, such methods are inapplicable to highly nonequilibrium dynamics (see however [13]), which represents one class of interesting problems in QCD, but essentially the entire class of interesting problems in strong-field QED (SFQED).

In the case of QCD, there has been considerable effort in recent years to develop quantum simulation techniques—methods for studying real-time dynamics on a future quantum computer [14–26]. Quantum computers offer new opportunities and new challenges for studying strongly coupled quantum field theories [27–29]. Although at present no quantum computer has been used to perform a Hamiltonian simulation that unambiguously outperforms classical simulations, the pace of development is rapid, and simulation techniques have improved in parallel with technological advances. It is hoped that on a timescale less than one career they will converge, and quantum computing will join classical lattice QCD in the compendium of essential computational tools [30–33].

Real-time quantum simulation is also a natural line of attack on SFQED physics. In [34], we took the first steps toward developing quantum simulation techniques for tree-level SFQED, using light-front quantization in the momentum basis. This formulation shares kinship with the Tamm-Dancoff approach [35,36] and with the more recent Hamiltonian truncation program [37–39], within light-front quantization [40] and adapted for digital quantum computers [41–43]. In this work we consider quantum simulations of SFQED at loop level, where new issues of renormalization must be confronted, and the encoded Hilbert subspace must be greatly enlarged. We focus on the photon polarization (or helicity) flip process [2–4,44–49]. This is the microscopic process underlying "vacuum birefringence"; the quantum vacuum, exposed to intense light, behaves as a birefringent medium, which has a measurable effect on the propagation of probe light. There is significant experimental interest in observing vacuum birefringence [50–53], which can in principle also be used as a probe of physics beyond the standard model, including

*Contact author: pdraper@illinois.edu
†Contact author: luisdh2@illinois.edu
‡Contact author: anton.ilderton@ed.ac.uk

Published by the American Physical Society under the terms of the Creative Commons Attribution 4.0 International license. Further distribution of this work must maintain attribution to the author(s) and the published article's title, journal citation, and DOI. Funded by SCOAP³.

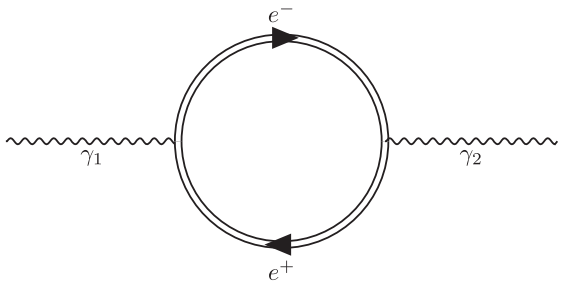


FIG. 1. One-loop Feynman diagram for polarization flip. A photon with given polarization encounters a background field; unlike in vacuum, the photon can flip to an orthogonal polarization state through the one-loop interaction shown. Fermions interact directly with the background, and the double line indicates that this interaction is accounted for nonperturbatively.

searching for minicharged particles [54] and hidden photons [55], see also Sec. 11.3 in [11].

The one-loop contribution to polarization flip is shown in Fig. 1. Our objective here is *not* to give new phenomenological insights into this process. Rather, polarization flip offers a natural next step beyond [34] because this process is (i) particularly simple in the class of background field we consider, where symmetries tightly constrain other degrees of freedom and (ii) related to that which we previously investigated—the imaginary part of the no-flip amplitude is, by the optical theorem, equal to the total probability of electron-positron pair production from an incident photon, in the background field (the nonlinear Breit-Wheeler process) [56].

We must emphasize that it is not at all obvious whether it is better to build quantum simulations of SFQED by working in momentum space or on a real spatial lattice [57]. Both have significant advantages and disadvantages. Momentum space has the advantage that it is easier to "carve out" the relevant Hilbert space and avoid wasting quantum resources. It is also the natural basis to use for computing observable scattering amplitudes. Disadvantages of momentum space include some nonlocality in the interactions and significant complications related to renormalization and symmetry. The real-space lattice approach essentially reverses most of these properties. In this work we focus exclusively on light-front quantization in momentum space and develop discretizations, truncations, and qubit encodings in this framework.

Hamiltonian renormalization on the light-front presents stimulating complications. The convenient light-cone gauge fixing and the natural regulators to use on a computer are noncovariant. This was first noted in [58], in light-front QED in the absence of background fields. Fortunately, a small number of counterterms is sufficient to restore the theory to the correct universality class.

One of our main results is the computation of A^2-counterterms in the presence of background fields. We compute one-loop amplitudes with hard momentum cutoffs in two scenarios: first, perturbatively, for general weak backgrounds, where we immediately recover the nonlocal counterterm of [58] for zero background, as well as corrections which are background-field dependent. Second, we consider the particular case of a (strong) "impulsive" plane wave background, which is both simple to work with analytically and the field for which we perform our classical and quantum simulations. Here we obtain the modified counterterms exactly, i.e. to all orders in the background.

This paper is organized as follows. In Sec. II we introduce the light-front Hamiltonian relevant to one-loop vacuum polarization processes. In Sec. III we calculate the one-loop amplitudes for polarization (no) flip and identify unphysical terms which arise due to the necessity of simulations requiring noncovariant cutoffs. We then find and discuss the appropriate counterterms to be added to the Hamiltonian. In Sec. IV we perform a classical Hamiltonian simulation. In Sec. V we discuss the resources needed to simulate this process on quantum computers. We conclude in Sec. VI.

A. Notation and conventions

In this paper, we use light-front coordinates [59–61] throughout. Four-vectors take the form $X^\mu = (X^+, X^-, X^1, X^2) \equiv (X^+, X^-, X^\perp)$, where $X^\pm = X^0 \pm X^3$. Meanwhile, $X_\mu = (X_+, X_-, X_\perp) = (\frac{X^-}{2}, \frac{X^+}{2}, -X^\perp)$. If x^μ and p^μ are coordinate and momentum four-vectors, then we take x^+ to be the light-front time coordinate and p^- to be the light-front energy. We avoid the zero mode [62,63] and only use $p^\pm > 0$.

It is convenient to define three-vectors $\mathsf{x} = (x^-, x^1, x^2)$ and $\mathsf{p} = (p^+, p^1, p^2)$. Additionally, we will write $d^3\mathsf{x} = dx^- dx^1 dx^2$ and $d^3\mathsf{p} = \theta(p^+) dp^+ dp^1 dp^2$. The on-shell dispersion relation for free particles is given by

$$p^- = \frac{p^\perp p^\perp + m^2}{p^+}, \tag{1}$$

in which repeated "$\perp$" indices are always summed over, and p^- is the light-front energy. (Set $m = 0$ for photons.)

Finally, we work in natural units with $\hbar = c = 1$ and report values in MeV. $m = 0.511$ MeV is the mass of the electron and $e = 0.303$ is chosen as the standard coupling value.

II. ONE-LOOP MOMENTUM-SPACE HAMILTONIAN

The SFQED Lagrangian density is

$$\mathcal{L} = -\frac{1}{4} F_{\mu\nu} F^{\mu\nu} + \bar{\psi}(i\partial\!\!\!/ - eA\!\!\!/ - e\mathcal{A}\!\!\!/ - m)\psi, \tag{2}$$

in which $\mathcal{A}^\mu$ is the background-field potential. We will take this background to be a plane wave propagating in the $-\hat{z}$

direction. The wave may be parametrized by the two transverse components $\mathcal{A}^i(x^+)$, while $\mathcal{A}^\pm = 0$.

The dependence of the background on light-front time x^+ makes it natural to work in light-front quantization. The corresponding Hamiltonian density $\mathcal{H}$ can be derived with the usual Legendre transform. The equations of motion yield constraints on the fermion and photon fields that can, unlike in "equal-time" quantization, be solved explicitly and substituted back into $\mathcal{H}$ [64]. Essentially, by solving Gauss's law and fixing light-front gauge $A^+ = 0$, we end up with an entirely physical Hilbert space—all states will satisfy Gauss's law. The resulting Hamiltonian depends on the dynamical fields A^i, i.e. the transverse components of A^μ, and on ψ_-, a projection of the original fermion field ψ having only two nonzero components; explicitly $\psi_- = \frac{1}{4}\gamma^-\gamma^+\psi$. The "price paid" for being able to work only with these unconstrained fields is that the Hamiltonian contains several new structures. Explicitly:

$$
\begin{aligned}
H = \frac{1}{2}\int d^3\mathsf{x}\Bigg(&\frac{i}{2}\psi_-^\dagger\frac{[(\partial_i + ie\mathcal{A}_i)^2 - m^2]\psi_-}{\partial_-} + e\mathcal{A}^-\psi_-^\dagger\psi_- - \frac{1}{2}A^i\partial_\perp^2 A^i \\
&+ \frac{e}{2}\partial_i A^i\frac{\psi_-^\dagger\psi_-}{\partial_-} - \frac{e}{2}\psi_-^\dagger\psi_-\frac{\partial_i A^i}{\partial_-} + \frac{iem}{2}\psi_-^\dagger\gamma^i A_i\frac{\psi_-}{\partial_-} - \frac{iem}{2}\psi_-^\dagger\gamma^i\frac{A_i\psi_-}{\partial_-} + \frac{e}{2}\psi_-^\dagger\gamma^i\gamma^j\frac{\partial_i(A_j\psi_-)}{\partial_-} + \frac{e}{2}\psi_-^\dagger\gamma^i\gamma^j A_i\frac{\partial_j\psi_-}{\partial_-} \\
&+ \frac{ie^2}{2}\psi_-^\dagger\gamma^i\gamma^j A_i\frac{A_j\psi_-}{\partial_-} - \frac{e^2}{2}\psi_-^\dagger\psi_-\frac{\psi_-^\dagger\psi_-}{\partial_-^2} + \frac{ie^2}{2}\psi_-^\dagger\gamma^i\gamma^j\mathcal{A}_i\frac{A_j\psi_-}{\partial_-} + \frac{ie^2}{2}\psi_-^\dagger\gamma^i\gamma^j A_i\mathcal{A}_j\frac{\psi_-}{\partial_-}\Bigg).
\end{aligned}
\tag{3}
$$

Expressions of the form $f(x^-)/\partial_-$ are Green's functions that come from solving the constraint equations for $\psi_+ = \frac{1}{4}\gamma^+\gamma^-\psi$ and A^- and are common in light-front calculations [59,61]. They can be understood as contributing, in momentum space, factors of $f(p^+)/(\pm ip^+)$.

The first line of (3) contains only "free" terms—free in the sense that they are quadratic in the quantized fields, but describe nontrivial interactions between the fermions and the background $\mathcal{A}$. The second line contains three-point vertices and are the same as in light-front QED without background. The first two terms of the third line are the instantaneous (in light-front time) two-photon-two-fermion interaction and the instantaneous four-fermion interaction. They are consequences of solving the field constraint solutions and again have the same form as without background. These will also be neglected below since they do not contribute to the processes of interest here [45]. The last two terms of the third line are effectively three-point vertices in terms of the *quantized* fields, corrected by the background. These are retained in what follows.

We will work in a particular interaction picture—the Furry picture [65]—in which the first line of (3), containing the interaction of fermions with only the background, is treated exactly as a free Hamiltonian $H_0(x^+)$, while the remainder of (3) constitutes the interaction Hamiltonian $V(x^+)$. The free part is, written out in terms of mode operators,

$$
\begin{aligned}
H_0(x^+) = &\int\frac{d^3\mathsf{p}}{(2\pi)^3}\sum_{s=\pm\frac{1}{2}}\left[\frac{(p^i - e\mathcal{A}^i(x^+))^2 + m^2}{p^+}\right]a_\mathsf{p}^{s\dagger}a_\mathsf{p}^s + \int\frac{d^3\mathsf{q}}{(2\pi)^3}\sum_{s=\pm\frac{1}{2}}\left[\frac{(q^i + e\mathcal{A}^i(x^+))^2 + m^2}{q^+}\right]b_\mathsf{q}^{s\dagger}b_\mathsf{q}^s \\
&+ \int\frac{d^3\mathsf{k}}{(2\pi)^3}\sum_{\lambda=1,2}k^- c_\mathsf{k}^{\lambda\dagger}c_\mathsf{k}^\lambda,
\end{aligned}
\tag{4}
$$

in which repeated indices are always summed over, and the ladder operators $a_\mathsf{p}^{s\dagger}/a_\mathsf{p}^s$, $b_\mathsf{q}^{s\dagger}/b_\mathsf{q}^s$, and $c_\mathsf{k}^{\lambda\dagger}/c_\mathsf{k}^\lambda$ describe electrons with helicity $-s$ and three-momentum p, positrons with helicity s and momentum q, and photons with polarization λ and momentum k, respectively.

Turning to the interaction part, we neglect terms as described above, along with further three-point terms which do not contribute, namely the $e^\pm \leftrightarrow e^\pm + \gamma$ (photon emission/absorption) terms. What remains is

$$
\begin{aligned}
V(x^+) = e\int\frac{d^3\mathsf{k}}{(2\pi)^3\sqrt{k^+}}\int\frac{d^3\mathsf{p}}{(2\pi)^3}\sum_{\lambda=1,2}\sum_{s=\pm\frac{1}{2}}\Bigg\{&-m\epsilon_\lambda^j R^{-s,j}\left(\frac{1}{p^+}+\frac{1}{q^+}\right)a_\mathsf{p}^{s\dagger}b_\mathsf{q}^{s\dagger}c_\mathsf{k}^\lambda + m\bar{\epsilon}_\lambda^i R^{s,i}\left(\frac{1}{p^+}+\frac{1}{q^+}\right)c_\mathsf{k}^{\lambda\dagger}b_\mathsf{q}^s a_\mathsf{p}^s \\
&+\epsilon_\lambda^j\left[\frac{p^{r'}-e\mathcal{A}^{r'}}{p^+}G^{-s,r',j} + \frac{q^{r'}+e\mathcal{A}^{r'}}{q^+}G^{-s,j,r'} + \frac{2k^j}{k^+}\right]a_\mathsf{p}^{-s\dagger}b_\mathsf{q}^{s\dagger}c_\mathsf{k}^\lambda + \bar{\epsilon}_\lambda^i\left[\frac{p^r-e\mathcal{A}^r}{p^+}G^{s,i,r} + \frac{q^r+e\mathcal{A}^r}{q^+}G^{s,r,i} + \frac{2k^i}{k^+}\right]c_\mathsf{k}^{\lambda\dagger}b_\mathsf{q}^{-s}a_\mathsf{p}^s\Bigg\}
\end{aligned}
\tag{5}
$$

in which, from here on, momentum conservation fixes $\mathsf{q} = \mathsf{k} - \mathsf{p}$ for each Hamiltonian operator. $R^{s,j}$ and $G^{s,j,k}$ take the values ± 1 or $\pm i$ only; working in the chiral basis of gamma matrices they are computed by

$$R^{s,j} = w^{-s\dagger}\gamma^j w^s, \qquad G^{s,j,k} = w^{s\dagger}\gamma^j\gamma^k w^s, \tag{6}$$

in which the w are a spinor basis, $w^{(+\frac{1}{2})} = (0,1,0,0)$, $w^{(-\frac{1}{2})} = (0,0,1,0)$. Finally, ϵ^i_λ are a linear basis for the (transverse) polarization of the photon,

$$\epsilon^i_1 = (1,0) \qquad \epsilon^i_2 = (0,1) \tag{7}$$

throughout. The creation and annihilation operators obey the usual (anti)commutation relations

$$\begin{aligned}\{a^s_{\mathsf{p}}, a^{s'\dagger}_{\mathsf{p}'}\} &= (2\pi)^3\delta_{ss'}\delta^3(\mathsf{p}-\mathsf{p}')\\ \{b^s_{\mathsf{q}}, b^{s'\dagger}_{\mathsf{q}'}\} &= (2\pi)^3\delta_{ss'}\delta^3(\mathsf{q}-\mathsf{q}')\\ [c^\lambda_{\mathsf{k}}, c^{\lambda'\dagger}_{\mathsf{k}'}] &= (2\pi)^3\delta_{\lambda\lambda'}\delta^3(\mathsf{k}-\mathsf{k}'),\end{aligned} \tag{8}$$

and create Fock states of particles.

III. AMPLITUDES, RENORMALIZATION AND COUNTERTERMS

In this section we compute the one-loop helicity flip and no-flip amplitudes for a photon, momentum k_μ, colliding with a general plane wave. We assume a head-on collision, taking $k_\mu = (k^+, 0, 0, 0)$. We use old-fashioned perturbation theory in the Furry (interaction) picture for this calculation, since this echoes the form of the numerical calculations performed later. The interaction $V(x^+)$ thus becomes the Furry-picture interaction Hamiltonian $H_V(x^+)$; the transformation from V to H_V is given by the operator replacement $[ab] \to [ab]e^{-i\Phi}$, with "Volkov" phase [66]

$$\Phi(p,x^+) = \frac{1}{2}\left(\frac{1}{p^+}+\frac{1}{q^+}\right)\int_0^{x^+} dz^+[(p^1 - e\mathcal{A}^1(z^+))^2 + (p^2 - e\mathcal{A}^2(z^+))^2 + m^2]. \tag{9}$$

To compute a second-order contribution to a scattering amplitude we require the time evolution operator

$$U_V(+\infty,-\infty) = 1 - \frac{i}{2}\int_{-\infty}^{+\infty} dy^+ H_V(y^+) - \frac{1}{4}\int_{-\infty}^{+\infty} dy_1^+ \int_{-\infty}^{y_1^+} dy_2^+ H_V(y_1^+)H_V(y_2^+) + \cdots. \tag{10}$$

The relation between U_V and the Schrödinger-picture time evolution operator, U, is $U_V = U_0^\dagger U$, where U_0 is a time evolution operator derived with the free Hamiltonian H_0. Because H_0 is entirely diagonal in the Fock basis, U_0 simply applies a phase to Fock final states, which drops out of our probabilities.

The polarization flip probability is

$$|\langle^{(2)}_k\gamma|\hat{U}_V(+\infty,-\infty)|\gamma^{(1)}_k\rangle|^2. \tag{11}$$

The relevant part of the time evolution operator for $\gamma^{(1,2)}_k \to \gamma^{(1,2)}_k$ is

$$\hat{U}_V(+\infty,-\infty) = 1 - \frac{e^2}{4}\int\frac{d^3\mathsf{k}}{(2\pi)^3 k^+}\sum_{\lambda,\lambda'=1,2}\bar{\epsilon}^i_{\lambda'}\Pi^{ij}\epsilon^j_\lambda c^{\lambda'\dagger}_{\mathsf{k}}c^\lambda_{\mathsf{k}} \tag{12}$$

where the on-shell polarization tensor Π^{ij} has the explicit form [45]

$$\begin{aligned}\Pi^{ij} = 2\int\frac{d^3\mathsf{p}}{(2\pi)^3}\int_{-\infty}^{+\infty} dy_1^+\int_{-\infty}^{y_1^+} dy_2^+ e^{-i\Phi(p,y_1^+)}e^{i\Phi(p,y_2^+)}\\ \times\left\{m^2\left(\frac{1}{p^+}+\frac{1}{q^+}\right)^2\delta_{ij} + \left(\frac{1}{p^+}+\frac{1}{q^+}\right)^2(p^r - e\mathcal{A}^r(y_1^+))(p^r - e\mathcal{A}^r(y_2^+))\delta_{ij}\right.\\ + \left(\frac{1}{p^+}-\frac{1}{q^+}\right)^2(p^i - e\mathcal{A}^i(y_1^+))(p^j - e\mathcal{A}^j(y_2^+)) - \left.\left(\frac{1}{p^+}+\frac{1}{q^+}\right)^2(p^j - e\mathcal{A}^j(y_1^+))(p^i - e\mathcal{A}^i(y_2^+))\right\},\end{aligned} \tag{13}$$

in which, here and below, the "cut" integral sign denotes the presence of a factor $\theta(k^+ - p^+)$ in the integrand. Note that $i \neq j$ ($i = j$) corresponds to the linear-polarization flip (no-flip) amplitude.

We expect UV divergences at loop level. For the one-loop helicity (no-) flip amplitudes these are dealt with by (i) regularizing the integrals and (ii) subtracting the free-field contributions (the latter carry all the divergences). This assumes a covariant momentum regularization scheme. There are, here, two relevant caveats which we now discuss.

First, regularization in simulations is achieved by essentially noncovariant means, i.e. hard momentum cutoffs are imposed, resulting in the explicit breaking of spacetime symmetries and gauge structure. Second, simulations in which we evolve an initial photon through discrete time steps will allow for polarization flip (or not) at each step, in other words a simulation does not compute a single amplitude, but rather a state. We must therefore renormalize in such a way that unwanted UV and symmetry-breaking effects are removed from the state. In a Wilsonian effective action obtained by integrating out UV quantum fluctuations, symmetry-breaking effects become encoded in local effective operators (which are particularly problematic if they are marginal or relevant). To deal with this, we can add counterterms to the bare Hamiltonian and tune them to cancel the unwanted effects of breaking due to the cutoff. We will see below that such operators are indeed generated in our system, and we will discuss the counterterms in details. To begin, we examine the polarization tensor in a specific choice of plane wave background which admits the most explicit calculations, and for which we will later perform both classical and quantum simulations.

A. Delta pulses

It is convenient to work with delta pulses [67–69], in which the electric and magnetic fields are (sequences of) delta functions in light-front time. These ultrashort pulses can be thought of as infinite-frequency limits of narrow-width plane waves. For our purposes, the primary benefit of using delta pulses is that the required scattering amplitudes (and counterterms) have very explicit forms, giving us concrete results against which to compare our numerics. For a discussion of the advantages and disadvantages of delta pulses as a physical model, see [68]. Furthermore, see Sec. III B where we consider more general, smoothly varying background fields.

We use the background potential

$$e\mathcal{A}^1(x^+) = e\mathcal{A}^2(x^+) = m\xi(\theta(x^+) - \theta(x^+ - T)), \quad (14)$$

which corresponds to an initial delta pulse at $x^+ = 0$, followed by a second pulse of equal magnitude and opposite sign at $x^+ = T$. This magnitude is characterized by the dimensionless and tunable parameter ξ, which is proportional to the classical work done on an electron by the background; an electron of initial momentum $\{p^+, p^i\}$ encountering the first delta pulse would be kicked to momentum $\{P^+, P^i\}$ with

$$P^i = p^i - m\xi, \qquad P^+ = p^+, \quad (15)$$

a notation we adopt from here on to compactify expressions.

Π^{ij} contains only two tensor structures: δ^{ij} for the no-flip amplitude $\mathcal{N}$, and $\mathcal{E}^{ij} = \epsilon_1^{(i}\epsilon_2^{j)}$ for the flip amplitude $\mathcal{F}$ (without a factor of $\frac{1}{2}$ in the symmetrization). Thus we can write

$$\Pi^{ij} = \delta^{ij}\mathcal{N} + \mathcal{E}^{ij}\mathcal{F}. \quad (16)$$

The flip amplitude $\mathcal{F}$ has both physical and unphysical terms. The physical piece is [69]

$$\mathcal{F} \supset -8\int \frac{d^3\mathsf{p}}{(2\pi)^3}\frac{4q^+}{k^+}\left[\frac{P^1}{P^-} - \frac{p^1}{p^-}\right]\left[\frac{P^2}{P^-} - \frac{p^2}{p^-}\right] \times \left[\frac{1 - e^{-ik^+P^-T/(2q^+)}}{p^+k^+}\right]. \quad (17)$$

This is the expression we use, below, to infer ideal Hamiltonian simulation parameters. The unphysical contribution is

$$\mathcal{F} \supset \frac{16iT}{k^+}\int \frac{d^3\mathsf{p}}{(2\pi)^3}\frac{P^1P^2}{P^\perp P^\perp + m^2}. \quad (18)$$

It is straightforward to see that this contribution depends on how the integral is regulated. It can be canceled by a counterterm which, we note, will depend on ξ. A third, seemingly divergent, contribution vanishes due to the residual symmetries of the cutoffs:

$$\mathcal{F} \supset \left(\int_{-\infty}^{0} dy_1^+ + \int_T^{+\infty} dy_1^+\right)\frac{16i}{k^+} \int \frac{d^3\mathsf{p}}{(2\pi)^3}\frac{p^1p^2}{p^\perp p^\perp + m^2} = 0. \quad (19)$$

Turning to the no-flip amplitude (and again using residual symmetries to simplify expressions), we identify two contributions exhibiting unphysical cutoff effects:

$$\mathcal{N} \supset -4i\left(\int_{-\infty}^{+\infty} dy_1^+\right)\int \frac{d^3\mathsf{p}}{(2\pi)^3} \times \left[\frac{k^+}{p^+q^+} - \frac{2}{k^+}\frac{p^\perp p^\perp}{p^\perp p^\perp + m^2}\right], \quad (20)$$

$$\mathcal{N} \supset \frac{8iT}{k^+}\int \frac{d^3\mathsf{p}}{(2\pi)^3}\left[\frac{P^\perp P^\perp}{P^\perp P^\perp + m^2} - \frac{p^\perp p^\perp}{p^\perp p^\perp + m^2}\right]. \quad (21)$$

Equation (20) is independent of both ξ and T, while (21) has an overall factor of T, similar to (18). Observe that both (18) and (21) vanish if the background is turned off ($\xi \to 0$) and would also vanish at nonzero ξ if the integrals could be regulated to preserve transverse translation invariance. We write down the counterterms required to remove unwanted effects below.

1. Counterterms

The unphysical effects identified above break spacetime symmetries and violate the constraint algebra of QED in the Hamiltonian formalism. We discuss these violations in more detail in the Appendix, but here we focus on removing them via the addition of counterterms. The counterterms are to be associated with operators of the form AA, with a background-dependent coefficient function. We therefore define a counterterm Hamiltonian H^c for the delta-pulse background to be

$$H^c = \frac{1}{2}\int d^3\mathsf{x}\, C_{ij}[\mathcal{A}]A^iA^j, \tag{22}$$

where

$$\frac{1}{2}\int d^3\mathsf{x}A^iA^j = \int \frac{d^3\mathsf{k}}{(2\pi)^3 k^+}\sum_{\lambda,\lambda'=1,2}\left(\epsilon^i_{\lambda'}\bar{\epsilon}^j_{\lambda}c^{\lambda\dagger}_{\mathsf{k}}c^{\lambda'}_{\mathsf{k}} + \bar{\epsilon}^i_{\lambda'}\epsilon^j_{\lambda}c^{\lambda'\dagger}_{\mathsf{k}}c^{\lambda}_{\mathsf{k}}\right). \tag{23}$$

C_{ij} is chosen to cancel the unphysical contributions detailed above. We read from (20), (21) and (18) that

$$\begin{aligned} C_{ij}[\mathcal{A}] = {}& \delta_{ij}e^2\int\frac{d^3\mathsf{p}}{(2\pi)^3}\left[\frac{k^+}{p^+q^+} - \frac{2}{k^+}\frac{p^\perp p^\perp}{p^\perp p^\perp + m^2}\right] \\ & - \delta_{ij}\Theta\frac{2e^2}{k^+}\int\frac{d^3\mathsf{p}}{(2\pi)^3}\left[\frac{P^\perp P^\perp}{P^\perp P^\perp + m^2} - \frac{p^\perp p^\perp}{p^\perp p^\perp + m^2}\right] \\ & - \mathcal{E}_{ij}\Theta\frac{4e^2}{k^+}\int\frac{d^3\mathsf{p}}{(2\pi)^3}\frac{P^1P^2}{P^\perp P^\perp + m^2}, \end{aligned} \tag{24}$$

where Θ is shorthand for the difference of step functions in the potential (14). The first line of (24) is the same nonlocal counterterm as found in [58] for QED without background and quantized on the light front (which serves as a minor consistency check on our calculations so far). The second and third lines are the field-dependent terms which only contribute between the delta pulses, and thus recover the factors of T in (21) and (18). Note that factors of $\frac{1}{k^+}$ are ultimately canceled by the p^+ integral.

For simulations it is practical to evaluate the above integrals (or Riemann sums) numerically for finite Λ. However, it is also possible to compute them analytically in powers of $\frac{m}{\Lambda}$, which we record here. We find

$$\frac{1}{2}\int_{-\Lambda}^{\Lambda} d^2p^\perp \frac{p^\perp p^\perp}{p^\perp p^\perp + m^2} \approx 2\Lambda^2 + m^2\left(2G + \pi\ln\left(\frac{m}{2\Lambda}\right)\right) \tag{25}$$

which contributes to the field-independent term, and

$$\begin{aligned} & \int_{-\Lambda}^{\Lambda} d^2p^\perp \frac{P^1P^2}{P^\perp P^\perp + m^2} \\ & \approx 2(m\xi)^2 - \frac{2(m\xi)^4 + 3m^2(m\xi)^2}{3\Lambda^2} \\ & \frac{1}{2}\int_{-\Lambda}^{\Lambda} d^2p^\perp\left[\frac{P^\perp P^\perp}{P^\perp P^\perp + m^2} - \frac{p^\perp p^\perp}{p^\perp p^\perp + m^2}\right] \\ & \approx \frac{m^2(\pi+2)}{2\Lambda^2}(m\xi)^2 \end{aligned} \tag{26}$$

where G is Catalan's constant.

B. Effective field theory

The unphysical contributions to the polarization tensor obtained above, and their counterterms, were computed for the specific background (14). The breaking of symmetries by cutoffs is not, however, particular to this background. Before moving on to numerical simulations using delta pulses, we therefore briefly investigate the form of counterterms required in more general cases, namely general plane wave fields.

Observe first that in the delta-pulse case above, the counterterms are all-orders in ξ, but their field-dependent parts have perturbative expansions beginning at $\mathcal{O}(\xi^2)$. This, combined with the theta functions present in (24), implies that to leading order in a weak-field expansion, the field-dependent counterterms originate from effective operators of the form $AA\mathcal{A}\mathcal{A}$. We therefore proceed with an effective field theory approximation, expanding in *weak fields and slow variations*. Clearly this second assumption excludes the delta-pulse case above, so we should not expect to find exact agreement with (the weak-field limit of) the counterterms above, but we will see similar structures appearing.

For convenience define

$$\begin{aligned} B_1^\ell(x^+) &= \int_0^{x^+} dz^+ e\mathcal{A}^\ell(z^+) \\ B_2(x^+) &= \int_0^{x^+} dz^+ e^2\mathcal{A}^\ell(z^+)\mathcal{A}^\ell(z^+) \end{aligned} \tag{27}$$

so that the phase factor (9) may be written

$$\begin{aligned} \Phi(p,x^+) = {}& \frac{p^- + q^-}{2}x^+ - \left(\frac{1}{p^+} + \frac{1}{q^+}\right)p^\ell B_1^\ell(x^+) \\ & + \frac{1}{2}\left(\frac{1}{p^+} + \frac{1}{q^+}\right)B_2(x^+). \end{aligned} \tag{28}$$

With this, we expand the product of phases $e^{-i\Phi(p,y_1^+)}e^{i\Phi(p,y_2^+)}$ appearing in the polarization tensor (13) up to quadratic order in $e\mathcal{A}^i$. This leaves a phase of $e^{i\frac{p^-+q^-}{2}(y_2^+-y_1^+)}$. Integrals containing this phase will of course be dominated by regions of slow oscillation, to identify which we note that

$$\frac{p^-+q^-}{2}(y_2^+-y_1^+)\lesssim 1 \Longleftrightarrow (y_2^+-y_1^+)m \lesssim 2\left[\frac{p^+q^+}{(k^+)^2}\right]\times\left[\frac{k^+m}{p^\perp p^\perp+m^2}\right]. \tag{29}$$

The first factor in square brackets is $\leq\frac{1}{4}$. If we assume $k^+\sim m$, then the second square-bracketed factor is $\lesssim 1$. It follows that for all loop momenta the phase oscillates rapidly unless $(y_2^+-y_1^+)<\frac{1}{m}$, which justifies a light-front time-derivative expansion of background fields under the time integrals, as long as the background fields are slowly varying compared to the Compton wavelength. Near the extremes $p^+\to 0$ and $p^+\to k^+$, the approximations are even better, since then some energy is large and so y_2^+ and y_1^+ must be more localized. For effects that are generated by transverse momenta of order Λ, $y_2^+-y_1^+$ is also more localized.

Thus we proceed by Taylor expanding about $y_2^+=y_1^+$,

$$B_1^\ell(y_2^+)\approx B_1^\ell(y_1^+)+e\mathcal{A}^\ell(y_1^+)y_m^+ \quad B_2(y_2^+)\approx B_2^\ell(y_1^+)+e^2\mathcal{A}^\ell(y_1^+)\mathcal{A}^\ell(y_1^+)y_m^+ \tag{30}$$

where we henceforth use a change of variables: $y_p^+=y_2^++y_1^+$ and $y_m^+=y_2^+-y_1^+$. Neglecting derivatives of the background field, we will approximate $e\mathcal{A}^i(y_2^+)\approx e\mathcal{A}^i(y_1^+)$.

With this procedure, we obtain

$$\Pi^{ij}_{(i\neq j)}=\frac{32i}{(2\pi)^3}\frac{1}{2+\frac{m^2}{\Lambda^2}}\int_{-\infty}^{+\infty}dy_p^+e^2\mathcal{A}^i\left(\frac{y_p^+}{2}\right)\mathcal{A}^j\left(\frac{y_p^+}{2}\right) \tag{31}$$

for $i\neq j$ and

$$\begin{aligned}\Pi^{ij}_{(i=j)}=&-2i\delta_{ij}\int\frac{d^3\mathsf{p}}{(2\pi)^3}\int_{-\infty}^{+\infty}dy_p^+\left\{\frac{k^+}{p^+q^+}-\frac{2}{k^+}\frac{p^\perp p^\perp}{p^\perp p^\perp+m^2}\right\}\\&+\frac{16i}{(2\pi)^3}\int_{-\infty}^{+\infty}dy_p^+e^2\mathcal{A}^i\left(\frac{y_p^+}{2}\right)\mathcal{A}^i\left(\frac{y_p^+}{2}\right)\left\{\frac{1+2\frac{m^2}{\Lambda^2}}{\sqrt{\left(1+\frac{m^2}{\Lambda^2}\right)^3}}\arctan\left(\frac{1}{\sqrt{1+\frac{m^2}{\Lambda^2}}}\right)-\frac{1}{1+\frac{m^2}{\Lambda^2}}+\frac{1}{2+\frac{m^2}{\Lambda^2}}\right\}\\&+\frac{16i}{(2\pi)^3}\int_{-\infty}^{+\infty}dy_p^+e^2\mathcal{A}^{3-i}\left(\frac{y_p^+}{2}\right)\mathcal{A}^{3-i}\left(\frac{y_p^+}{2}\right)\left\{\frac{1}{2+\frac{m^2}{\Lambda^2}}-\frac{1}{\sqrt{1+\frac{m^2}{\Lambda^2}}}\arctan\left(\frac{1}{\sqrt{1+\frac{m^2}{\Lambda^2}}}\right)\right\}\end{aligned} \tag{32}$$

for $i=j$, to all orders in $\frac{m}{\Lambda}$. (Note the use of $y_m^+\to 0$, hence $y_1^+\to\frac{y_p^+}{2}$.) Expanding these amplitudes to $\mathcal{O}(\frac{m^2}{\Lambda^2})$ yields expressions analogous to those in (26).

As in the delta-pulse analysis, we observe in these expressions UV-finite (independent of Λ as $\Lambda\to\infty$) contributions associated with effective operators of the form AA and $AA\mathcal{A}\mathcal{A}$. This phenomenon appears to be a general deficiency of the hard momentum cutoffs that are most natural for numerical analysis. In contrast physical effects are associated with higher-order effective operators, in particular terms with more derivatives, and they can be derived by keeping more powers of $e\mathcal{A}^i$ and its derivatives in the Taylor expansions. Here we capture only the counterterms needed to remove the unphysical AA and $AA\mathcal{A}\mathcal{A}$ contributions.

We define a generalized counterterm Hamiltonian:

$$H^c=\frac{1}{4}\int d^3\mathsf{x}\Big(C_{AA}A_\mu A^\mu+C_{AA\mathcal{A}\mathcal{A}}(A_\mu A^\mu)(\mathcal{A}_\nu\mathcal{A}^\nu)+C_{2A\mathcal{A}}(A_\mu\mathcal{A}^\mu)^2+D_{\mu\nu\rho\sigma}A^\mu A^\nu\mathcal{A}^\rho\mathcal{A}^\sigma\Big). \tag{33}$$

After gauge fixing, this becomes

$$H^c=\frac{1}{4}\int d^3\mathsf{x}\Big(-C_{AA}A^iA^i+C_{AA\mathcal{A}\mathcal{A}}A^iA^i\mathcal{A}^j\mathcal{A}^j+C_{2A\mathcal{A}}A^iA^j\mathcal{A}^i\mathcal{A}^j+D_{ijk\ell}A^iA^j\mathcal{A}^k\mathcal{A}^\ell\Big). \tag{34}$$

Using our effective field theory calculations above, the counterterm coefficients are

$$
\begin{aligned}
C_{AA} &= -e^2 \int \frac{d^3\mathsf{p}}{(2\pi)^3}\left[\frac{k^+}{p^+q^+} - \frac{2}{k^+}\frac{p^\perp p^\perp}{p^\perp p^\perp + m^2}\right] \\
C_{AAAA} &= -\frac{8e^4}{(2\pi)^3}\left[\frac{1}{2+\frac{m^2}{\Lambda^2}} - \frac{1}{\sqrt{1+\frac{m^2}{\Lambda^2}}}\arctan\left(\frac{1}{\sqrt{1+\frac{m^2}{\Lambda^2}}}\right)\right] \\
C_{2AA} &= -\frac{8e^4}{(2\pi)^3}\left[\left(\frac{1+2\frac{m^2}{\Lambda^2}}{\sqrt{\left(1+\frac{m^2}{\Lambda^2}\right)^3}} + \frac{1}{\sqrt{1+\frac{m^2}{\Lambda^2}}}\right)\arctan\left(\frac{1}{\sqrt{1+\frac{m^2}{\Lambda^2}}}\right) - \frac{1}{1+\frac{m^2}{\Lambda^2}}\right] \\
D_{ijk\ell} &= -\mathcal{E}^{ij}\mathcal{E}^{k\ell}\left(\frac{8e^4}{(2\pi)^3}\frac{1}{2+\frac{m^2}{\Lambda^2}} + C_{2AA}\right).
\end{aligned} \tag{35}
$$

We remark that expansions analogous to those above lie behind the "locally constant field approximation," one of the central tools for linking SFQED predictions, simulations and experiments [70]. For a review see [67] and for discussions of the failings and extension of the approximation see [71,72].

IV. CLASSICAL SIMULATION

We now have counterterms that we can include into our Hamiltonian to remove unwanted cutoff effects during time evolution. We have also shown that these are consistent with the expected form of counterterms in more general fields. Therefore, "real-time" classical and quantum simulations alike should be robust against cutoff effects, as long as the counterterms are present in the time evolution operator. In simulations, this operator may be approximated [73] by the first-order time evolution Trotterization

$$
\begin{aligned}
U(x^+,x_0^+) &= \mathcal{T} e^{-\frac{i}{2}\int_{x_0^+}^{x^+} H(y^+)dy^+} \\
&= e^{-\frac{i}{2}H(x_n^+)\Delta x^+}\cdots e^{-\frac{i}{2}H(x_1^+)\Delta x^+} + \mathcal{O}[(\Delta x^+)^2]
\end{aligned} \tag{36}
$$

for n time steps of size $\Delta x^+ = \frac{x^+ - x_0^+}{n}$ and n times $x_0^+ < x_1^+ < \cdots < x_n^+ = x^+$, with $x_k^+ = k\Delta x^+ + x_0^+$.

We wish to compute the probability $|\langle {}^{(2)}_{k}\gamma | U(+\infty,-\infty)|\gamma^{(1)}_{k}\rangle|^2$ with Hamiltonian simulation [40,74,75] via Trotterization. To deal with the asymptotic limits, we perform an adiabatic time evolution. This splits the time evolution of the system into three regions: adiabatic turn-on (from $X^+_{\mathrm{on},i}$ to $X^+_{\mathrm{on},f}$), constant coupling (from $X^+_{\mathrm{on},f}$ to $X^+_{\mathrm{off},i}$), and adiabatic turn-off (from $X^+_{\mathrm{off},i}$ to $X^+_{\mathrm{off},f}$).

During adiabatic turn-on we begin in a single-photon Fock state, which is an eigenstate of H_0, the free Hamiltonian. We turn on the coupling $e(x^+)$ linearly during this interval. This allows us to approximately prepare an eigenstate of H, the full Schrödinger-picture Hamiltonian. During constant coupling, the interaction with the background field occurs. The coupling $e(x^+)$ is held constant. During adiabatic turn-off we linearly turn off the coupling $e(x^+)$. This returns the eigenbasis to Fock space. Thus, we can measure overlap with a final single-photon Fock state.

A. Hamiltonian truncation

To simulate on a computer, we must work with a finite Hilbert space. We include a tower of two-particle e^+e^- states, and *two* one-particle photon states, with polarization $\lambda = 1,\ 2$ and as above, momentum $k^\mu = (k^+,0,0,0)$ corresponding to a head-on collision between the incident photon and our plane wave. The restriction to *only* this momentum mode follows from the explicit results for the polarization and time evolution operators above and the symmetries of the plane wave background; while only three components of momentum are conserved, this is enough to fix the on-shell momentum of a single incoming photon. Internal degrees of freedom can still change due to interaction with the background, though, in particular the helicity of the photon.

We impose spatial periodic boundary conditions, hence momenta become discretized in steps of $2\pi/L_\perp$ and $2\pi/L_+$ for the transverse and longitudinal momenta, respectively. Electron momenta now appear as $\mathsf{p} = (\frac{2\pi n_+}{L_+}, \frac{2\pi n_1}{L_\perp}, \frac{2\pi n_2}{L_\perp})$ which we will abbreviate in function arguments to just $2\pi n/L$. Discretization turns integrals into Riemann sums,

$$
\begin{aligned}
\int \frac{d^3\mathsf{p}}{(2\pi)^3} F(p)[a] \to \sum_{n_+=1}^{+\infty}\sum_{n_1,n_2=-\infty}^{+\infty} \frac{1}{L_+L_\perp^2} \\
\times F\left(\frac{2\pi n}{L}\right)\left[\sqrt{L_+L_\perp^2}\,a\right],
\end{aligned} \tag{37}
$$

where $[a]$ denotes some single-particle operator that is scaled by $\sqrt{L_+L_\perp^2}$ when passing from the continuum to finite volume. To truncate the Hamiltonian, we impose cutoffs on the momentum modes. In the longitudinal

direction, we allow up to $K-1$ modes. In the transverse directions, we use symmetric cutoffs $\Lambda = \frac{2\pi N}{L_\perp}$ for $N \geq 0$:

$$\sum_{n_+=1}^{+\infty} \sum_{n_1,n_2=-\infty}^{+\infty} \frac{1}{L_+ L_\perp^2} F\left(\frac{2\pi n}{L}\right) \left[\sqrt{L_+ L_\perp^2}\, a\right] \to \sum_{n_+=1}^{K-1} \sum_{n_1,n_2=-N}^{N} \frac{1}{L_+ L_\perp^2} F\left(\frac{2\pi n}{L}\right) \left[\sqrt{L_+ L_\perp^2}\, a\right]. \tag{38}$$

For a given (K,N), the number of electron-positron pairs is $4(K-1)(2N+1)^2$, where the factor of four comes from counting spin/helicity.

We use the usual occupation number basis and order the states as

$$|\ldots, e^{-\left(+\frac{1}{2}\right)}_{\mathsf{p}_n}, \ldots, e^{-\left(-\frac{1}{2}\right)}_{\mathsf{p}_n}, \ldots, e^{+\left(+\frac{1}{2}\right)}_{\mathsf{q}_n}, \ldots, e^{+\left(-\frac{1}{2}\right)}_{\mathsf{q}_n}, \ldots, \gamma^{(1)}_{\mathsf{k}_n}, \ldots, \gamma^{(2)}_{\mathsf{k}_n}, \ldots\rangle. \tag{39}$$

Usually, a fermion creation and annihilation operator acts with a factor of $(-1)^\zeta$, where ζ is the sum of fermion occupation numbers to the left of the fermion acted on, relative to the ordering in (39). $[a^\dagger a]$- and $[b^\dagger b]$-type operators will always yield factors of $(-1)^{2\zeta} = 1$. Meanwhile, $[a^\dagger b^\dagger]$- and $[ba]$-type operators that appear in our normal-ordered Hamiltonian will act only on vacuum or electron-positron pair Fock states (in our eventual truncation). The $[b^\dagger]$ operator in $[a^\dagger b^\dagger]$ first acts on the vacuum, where $(-1)^\zeta \to 1$. Then $[a^\dagger]$ acts on a positron Fock state, but due to the ordering in (39), positron occupation numbers do not contribute to ζ for $[a^\dagger]$ operators. A similar situation occurs for $[ba]$. Therefore, the $(-1)^\zeta$ factor will always result in factors of one in our simulations and can be neglected.

B. Simulation parameters

Returning to the delta pulses, we seek appropriate parameters $\{\Lambda, K, N\}$ given inputs $\{T, k^+, \xi\}$. We choose $k^+ = m$ and $\xi = 1$, while $T \sim \mathcal{O}(\frac{1}{m})$. Note that choosing (K,N) fixes $L_+ = \frac{2\pi K}{k^+}$ and $L_\perp = \frac{2\pi N}{\Lambda}$.

We can numerically integrate (17) to get "exact" polarization flip probabilities. Then, by imposing our UV cutoff Λ, we calculate

$$-8 \int_0^{k^+} \frac{dp^+}{2\pi} \int_{-\Lambda}^{\Lambda} \frac{d^2p^\perp}{(2\pi)^2} \frac{4q^+}{k^+} \left[\frac{P^1}{P^-} - \frac{p^1}{p^-}\right] \times \left[\frac{P^2}{P^-} - \frac{p^2}{p^-}\right] \left[\frac{1 - e^{-ik^+P^-T/(2q^+)}}{p^+k^+}\right] \tag{40}$$

to obtain "cutoff" probabilities. We find that $\Lambda = 5m$ offers good agreement between exact and cutoff probabilities. This value for the cutoff is expected because the polarization flip process is UV finite. Hence, the cutoff is on the order of $m\xi$—the characteristic energy scale in the loop.

Next, we calculate the Riemann sum of (40) with (K,N):

$$-\frac{8}{L_+ L_\perp^2} \sum_{n_+=1}^{K-1} \sum_{n_i,n_j=-N}^{N} \frac{4q^+}{k^+} \left[\frac{P^1}{P^-} - \frac{p^1}{p^-}\right] \times \left[\frac{P^2}{P^-} - \frac{p^2}{p^-}\right] \left[\frac{1 - e^{-ik^+P^-T/(2q^+)}}{p^+k^+}\right] \Bigg|_{p^i \to \frac{2\pi n_i}{L_\perp}, p^+ \to \frac{2\pi n_+}{L_+}} \tag{41}$$

to get "cutoff and discretized" probabilities. We find that $(K,N) = (12,13)$ offers fair agreement with the cutoff probabilities. The momentum resolution $\frac{1}{L}$ should be at least an order of magnitude less than the relevant momenta, $k^+ = m$ and $m\xi = m$, in order to have a rough approximation to the continuum limit and avoid discretization effects when $\frac{1}{L}$ is on the order of k^+ or $m\xi$. Our values of $(L_+, L_\perp) \approx (\frac{16}{m}, \frac{75}{m})$ are consistent with this guideline.

Let us now quantify what we mean by "good/fair agreement." The cutoff and discretization are necessary in order to perform a practical simulation with finite resources, but they introduce errors. We set a tolerance of 10% on the fidelity between the simulation and the exact result; we consider any set of parameters for which the cutoff, discretized calculation is correct to within this tolerance equally accurate. However, some choice of parameters may be more expensive than others. When calculating (40) with various values of Λ, we chose one of the lowest integer multiples of m that kept the cutoff probability within the 10% tolerance of the exact probability for $T = 1, \ldots, 10$. When calculating (41) with various values of (K,N), we prioritized a high K and a low N, because the number of electron-positron pairs increases by a factor of KN^2. We chose the lowest value of N that admitted a practical value of K that kept the cutoff and discretized probability within 10% of the cutoff probability for $T = 1, \ldots, 10$. This complete analysis is summarized in Fig. 2.

We remark that for the background delta pulses we consider, we were fortunate to have analytical results such as (17). That is, we were able to perform the time integrals of (14) exactly. These perturbative expressions are very convenient to find suitable simulation parameters. For general background fields, it will be necessary to perform the time integrals of (14) numerically. If this is unfeasible, then an alternative method would be to perform Trotterized time evolution simulations (classical or quantum), varying the parameters each time, until some convergence is measured.

C. Results

All counterterms detailed in Sec. III A 1 must be implemented—even the no-flip ones. This is because

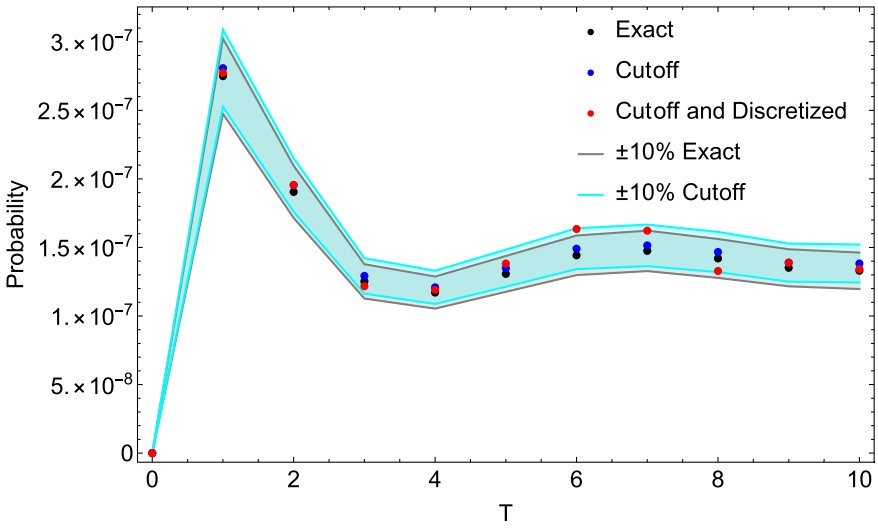


FIG. 2. Quantifying cutoff and discretization effects. We compare the accuracy of the cutoff polarization flip probability, calculated with (40) and $\Lambda = 5$ m, with the exact probability from (17). We also compare the cutoff and discretized probability, found with (41) and $(K, N) = (12, 13)$, with the cutoff probability. Here, $(k^+, \xi) = (m, 1)$ and the delta-pulse spacing T is varied. The band marked "±10% Exact" shows the window in which the exact probability varies by 10%. The band marked "±10% Cutoff" shows the same around the probability computed with the cutoff amplitude.

Hamiltonian simulation will produce more dynamics than Fig. 1 alone. For example, the simulation will allow processes such as $\gamma_1 \to \gamma_2 \to \gamma_1 \to \gamma_1 \to \cdots$. The counterterms are calculated numerically as Riemann sums. Figure 3 shows polarization flip probabilities for different values of T using Trotterization versus a cutoff and discretized perturbative scattering amplitude. Meanwhile, Fig. 4 shows the underlying "real-time" polarization flip probability for $T = 5$.

It is possible to check some of the broad features of Figs. 2 and 3 by analyzing the helicity flip amplitude (41) and in particular the phase factor

$$1 - e^{-ik^+P^-T/(2q^+)} \tag{42}$$

appearing there. For $T < 1$ a Taylor expansion about $T = 0$ leaves (42) proportional to T, hence the probability should grow roughly as T^2 for $T \ll 1$, which explains the initial

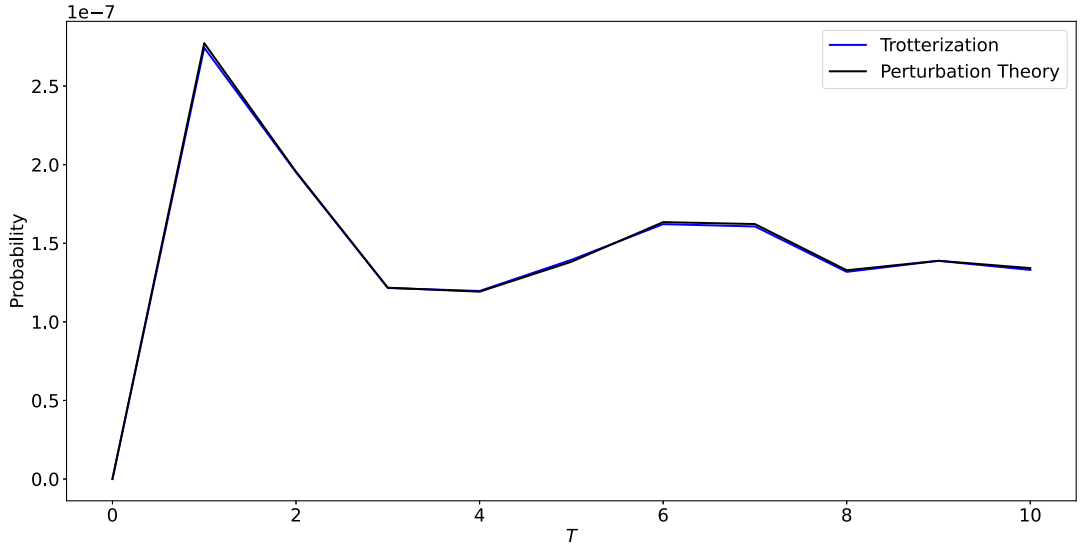


FIG. 3. Convergence of Trotter simulation and perturbation theory. The figure above compares polarization flip probabilities obtained from Trotterization versus cutoff and discretized perturbation theory for several values of T. Probabilities are obtained from the late-time state after a period of adiabatic turn-off of the coupling. See Fig. 4 for a sample simulation that produced the Trotterization data point at $T = 5$.

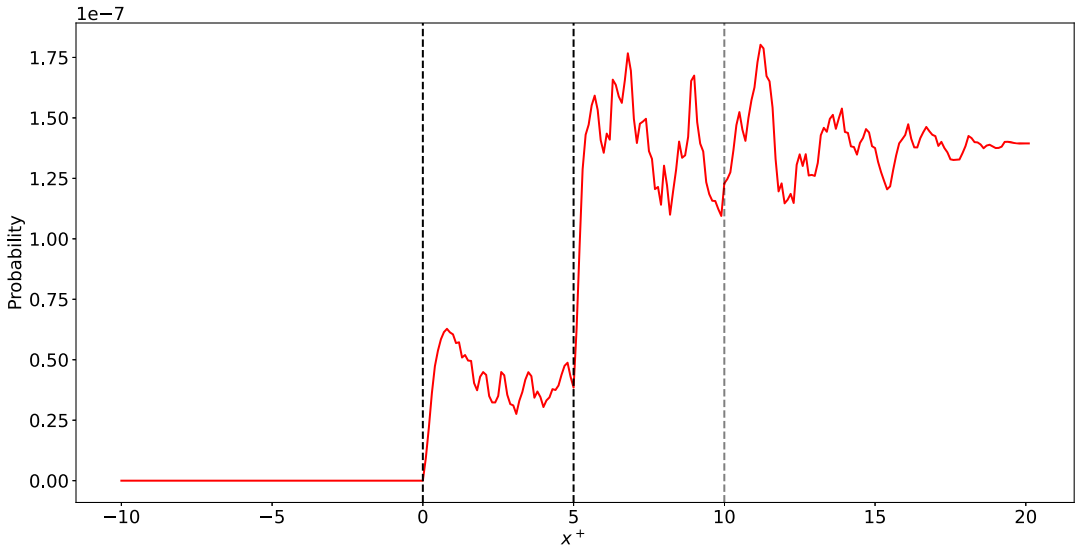


FIG. 4. Time-dependent polarization flip probabilities obtained from Trotterization. Here, $\Delta x^+ = 0.1$ and $T = 5$. Adiabatic turn-on starts at $x^+ = -10$ and ends at $x^+ = 0$. From $x^+ = 0$ to $x^+ = 10$, the coupling is held at $e = 0.303$. The black dashed lines show where an initial delta pulse appears at $x^+ = 0$ and is later canceled by an opposite-sign pulse at $x^+ = 5$. The gray dashed line shows when adiabatic turn-off begins, lasting until $x^+ = 20$ where $e = 0$.

rise in the polarization flip probability seen in Figs. 2 and 3. For $T \gtrsim 1$, though, the probability ceases to increase and instead develops oscillations. Now, the probability is (41) multiplied by its complex conjugate, both of which are sums over momenta. These sums interfere, and the dominant contributions to the probability should come from where the phase is slowly varying, corresponding to momentum configurations at which the exponent of (42) is minimized. The factor $1/(p^+q^+)$ is minimized when $p^+ = k^+/2$, and $|p^\perp| \sim m\xi$, so $P^\perp P^\perp = 0$. The exponent then becomes $2m^2T/k^+$. Interference effects begin to cause oscillations once the exponent reaches $\mathcal{O}(1)$, corresponding to $T \sim k^+/(2m^2)$. For the chosen parameter values in the figures, this is $T \sim 1/(2m) \approx 1\ \mathrm{MeV}^{-1}$, which indeed matches with the T at which oscillations set in.

It is worth noting that the numerical results shown in Figs. 2 and 3 agree well with the expected long-T behavior.

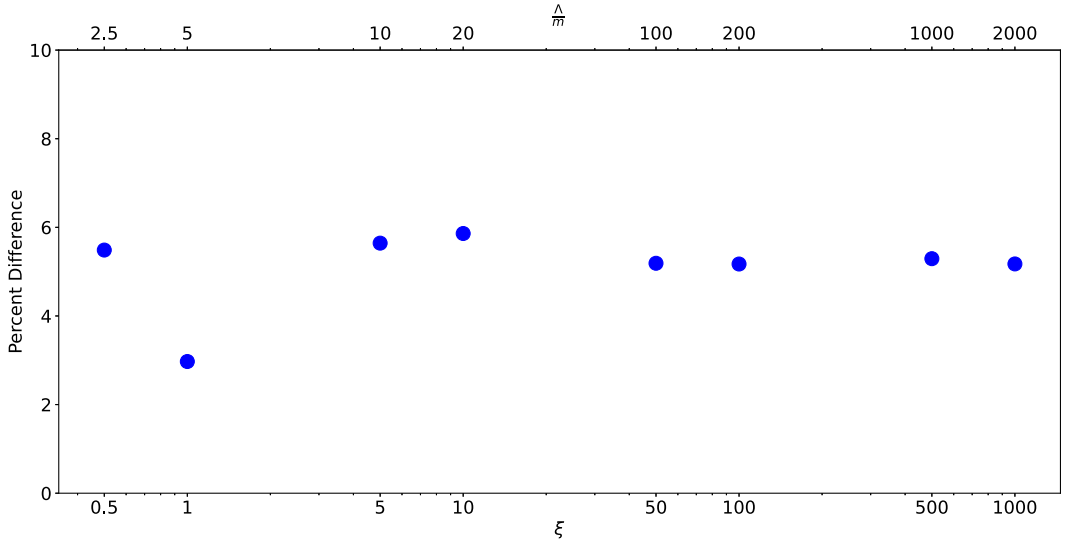


FIG. 5. Robustness of the discretization procedure to changes in background-field strength. This figure shows the percent difference of cutoff and discretized probabilities, averaged over a large-T interval, with the expected probabilities calculated with (43) for various values of ξ. $(K, N) = (12, 13)$ was kept fixed, but Λ was adjusted for each ξ. The value of ξ is shown on the lower horizontal axis, and the chosen value of Λ is shown on the upper horizontal axis in units of m. The cutoff and discretized probabilities were sampled from 500 equally spaced values of T between $T = 100$ and $T = 150$.

For large T, the phase in (17) can be dropped, and the polarization flip probability becomes

$$\lim_{T\to+\infty} |{}^2_k\langle\gamma|\hat{U}_V(+\infty,-\infty)|\gamma\rangle^1_k|^2 = \frac{e^4}{36\pi^4\xi^2}\left[\xi - \frac{2}{\sqrt{\xi^2+2}}\operatorname{arctanh}\left(\frac{\xi}{\sqrt{\xi^2+2}}\right)\right]^2. \quad (43)$$

With $\xi = 1$, this evaluates to about 1.38×10^{-7}. In Fig. 5, we further demonstrate the robustness of our simulation parameters to variations in ξ. There, we compare (43) with large-T cutoff and discretized probabilities computed with fixed (K, N), varying ξ. By choosing an appropriate Λ, it is seen that the percent difference between the two probabilities is relatively stable, suggesting that a choice of (K, N) is robust against changes in the background-field strength. Note that the cutoff and discretized probabilities are inherently noisy due to the sum—as opposed to integral—over complex phases. Therefore, an average was performed over a large-T interval to calculate sensible large-T cutoff and discretized probabilities.

V. QUANTUM SIMULATION

Quantum computers may one day be useful for simulating the large number of degrees of freedom found in a many-body quantum system. This is because their (typical) fundamental unit of information, the qubit, is itself a quantum system [76]. A qubit has two basis states: the $|0\rangle = \binom{1}{0}$ state and the $|1\rangle = \binom{0}{1}$ state, which are eigenstates of the Pauli Z operator.[1] When n qubits are brought together, their 2^n-dimensional Hilbert space can be described using the computational basis $\{|0\ldots0\rangle, |0,\ldots,1\rangle,\ldots,|1\ldots1\rangle\}$, which is a basis of tensor-product states. Therefore, if the target quantum system to be simulated has a Hilbert space with dimension d, then at least $n = \log_2\lceil d\rceil$ qubits are needed to encode the basis states of the target quantum system.

From here, most quantum computers work by applying norm-preserving unitary operators, called quantum gates, on qubits. (We direct the reader to [77] for a list of common quantum gates.) Note that most quantum gates act nontrivially on only a subset of the qubits; in fact, any quantum computation involving n qubits can be performed with only single-qubit and two-qubit gates. The complete product of quantum gates used in a quantum computation is called the quantum circuit. In this section we detail how the truncated Hilbert space in the polarization flip process may be encoded with qubits, as well as how the quantum circuit that implements the time evolution operator may be built for our encoding.

[1]In the quantum computing community it is common to denote the Pauli matrices σ^1, σ^2, σ^3 as X, Y, Z, respectively.

The Hamiltonian as formulated in Sec. II acts on Fock space, a convenient basis of which is the occupation number basis. Basis states appear in the form $|n_1 n_2 \cdots n_N\rangle$ for an N-particle system, where n_i labels the occupation number of the ith particle species. The total number of particles in a basis state is $\sum_i n_i$, in which $n_i = 0, 1$ for fermions and $n_i = 0, 1, 2, \ldots$ for bosons. For our quantum simulations, we will truncate the maximum photon occupation number to one, as we did in Sec. IV. Therefore, all remaining basis states are tensor products of N $|0\rangle$ and $|1\rangle$ states, which is exactly the form of a computational basis state for $n = N$ qubits. Thus, n qubits can encode the Fock space for n single-particle species, with each computational basis state corresponding to an occupation number basis state. Effectively, each qubit encodes the state of a specific particle species. For example, if $n = 3$, then $|000\rangle$ would be the vacuum state, $|001\rangle$ could be a single-photon state, and $|110\rangle$ could be an electron-positron pair state. The photon creation and annihilation operators appearing in the Hamiltonian are simply ladder operators that flip qubit basis states $|0\rangle \leftrightarrow |1\rangle$ or annihilate them. The fermion creation and annihilation operators, on the other hand, must be formulated to act on qubits so as to maintain their anticommutation relations.

The Jordan-Wigner transformation [78–80] is a commonly used tool to map fermionic operators to qubit operators. It requires each single-particle fermion state to be encoded with its own qubit, where $|0\rangle$ means the fermion is absent and $|1\rangle$ means the fermion is present. Fermionic anticommutation relations are upheld by attaching a tensor product of Z operators in front of the ladder operator according to a prescribed ordering of the fermions, as in (39). For the one-loop polarization flip process, we find this to be an unfeasible approach. Thousands of intermediate electron-positron pairs would require thousands of qubits—not currently available on quantum computers—to simulate. In the future, when large-scale fault-tolerant quantum computers become available, this may be the encoding of the Fock space necessary to simulate more general SFQED processes such as cascades. For now, it is too expensive to carry out a proof-of-principle quantum simulation of our polarization flip process with it.

Instead, we recognize that our Hamiltonian truncation leaves us with only electron-positron and single-photon Fock basis states. We can encode a total of d states with $n = \log_2\lceil d\rceil$ qubits, as described above. Then a computational basis state such as $|0011\rangle$, implying the use of four qubits, could encode (for example) some electron-positron pair when $8 < d \le 16$. However, such a dense binary encoding can lead to a rather expensive quantum circuit. The controlled unitaries detailed below would generally have to be controlled on all n qubits, which leads to more single- and two-qubit gates in their decomposition. In particular, more $\mathrm{T} = \sqrt[4]{Z}$ gates—deemed costly

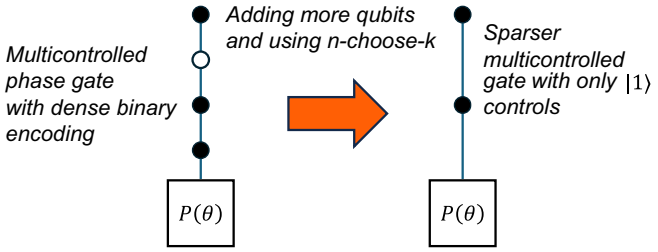


FIG. 6. Dense binary encoding versus n-choose-k encoding. The left phase gate is controlled on four qubits in a dense binary encoding. The right phase gate is controlled on $k-1=2$ qubits in an n-choose-k encoding. Suppose, for example, that $2^5=32$ states were encoded with the dense binary encoding. The n-choose-k encoding can encode up to $\binom{n}{k}$ states; therefore at least $n=7$ qubits would be needed to encode the same states with the n-choose-k encoding because there exists no k such that $\binom{n}{k}\geq 32$ for $n\leq 6$. For $n=7$, the minimum sufficient value of k is $k=3$, in which case $\binom{7}{3}=35$. The figure above could represent a reencoding $|10110\rangle\rightarrow|1001001\rangle$.

in fault-tolerant quantum computing for their difficulty to simulate classically—would be required.

To balance the number of qubits necessary[2] and the subsequent number of quantum gates we use what we call an "n-choose-k" encoding. (See Fig. 6 for a sketched comparison with the dense binary encoding.) Let F_i be the set of all Fock states that have a specific population "i" of particle species. For example, F_γ would be all single-photon Fock states and $F_{e^-e^+}$ would be all electron-positron pair Fock states. We designate n_i qubits for F_i. Then we choose $n_i\geq k_i>0$. States of F_i are then encoded by bit strings where all $F_{j\neq i}$ qubits are in the $|0\rangle$ state, and k_i of the n_i qubits are in the $|1\rangle$ state. This scheme encodes $\binom{n_i}{k_i}$ F_i states.

For our simulations, we fix $n_\gamma=2$ and choose $k_\gamma=1$. In particular,

$$|\gamma_k^{(1)}\rangle=|10\rangle\underbrace{|000\ldots000\rangle}_{F_{e^-e^+}\text{Qubits}}|\gamma_k^{(2)}\rangle=|01\rangle\underbrace{|000\ldots000\rangle}_{F_{e^-e^+}\text{Qubits}}. \tag{44}$$

Meanwhile, $n_{e^-e^+}$ and $k_{e^-e^+}$ can vary. This way we translate creation and annihilation operators into a tensor-product of ladder operators:

$$[c^\dagger ba]\sim|\gamma\rangle\langle e^-e^+|\rightarrow\sigma^+\otimes\underbrace{\sigma^-\otimes\cdots\otimes\sigma^-}_{k_{e^-e^+}} \tag{45}$$

or projectors:

$$[a^\dagger a],[b^\dagger b]\sim|e^-e^+\rangle\langle e^-e^+|\rightarrow\underbrace{\pi^1\otimes\cdots\otimes\pi^1}_{k_{e^-e^+}} \tag{46}$$

where n_i-k_i identity operators are implicit. Here, we use

$$\sigma^+=|1\rangle\langle 0|\quad\sigma^-=|0\rangle\langle 1|\quad\pi^0=|0\rangle\langle 0|\quad\pi^1=|1\rangle\langle 1|. \tag{47}$$

The n-choose-k encoding requires the knowledge of Hamiltonian matrix elements; these will be the time-dependent coefficients of the operators shown above. As such, any possible fermionic phase factors are baked into these elements, and so the fermionic anticommutation relations are directly imposed throughout the simulation.

We now have an encoding of our truncated Fock space and know how the Hamiltonian acts on the computational basis states. We move on to construct a quantum circuit for the time evolution operator that acts on the encoded qubits. To perform time evolution as in (36), we need the quantum gates that implement the unitary $e^{-\frac{i}{2}H(x_k^+)\Delta x^+}$. However, this is difficult to do exactly, so we use an additional first-order Trotterization[3]:

$$e^{-\frac{i}{2}H(x_k^+)\Delta x^+}=\prod_{h\in H_0(x_k^+)}e^{-\frac{i}{2}h\Delta x^+}\prod_{h\in V(x_k^+)}e^{-\frac{i}{2}h\Delta x^+}\prod_{h\in H^c(x_k^+)}e^{-\frac{i}{2}h\Delta x^+}+\mathcal{O}[(\Delta x^+)^2]. \tag{48}$$

Each h is a Hermitian operator that acts on two Fock states. For instance, $C|e^-e^+\rangle\langle e^-e^+|$ and $C|e^-e^+\rangle\langle\gamma|+C^*|\gamma\rangle\langle e^-e^+|$ are examples of h operators. Now we turn to the problem of finding the quantum gates that implement each $e^{-\frac{i}{2}h\Delta x^+}$.

In the free Hamiltonian, the only operators are of the type $C|e^-e^+\rangle\langle e^-e^+|$. The matrix exponential of a string of projectors is a multicontrolled phase gate as shown in Fig. 7. The phase gate $P(\theta)=e^{i\theta\pi^1}$ applies a phase of $e^{i\theta}$ on $|1\rangle$ but leaves $|0\rangle$ alone.

In the interaction Hamiltonian, the operators drive transitions between electron-positron pairs and photons. They appear as $C|e^-e^+\rangle\langle\gamma|+C^*|\gamma\rangle\langle e^-e^+|$, where C is a complex coefficient. The matrix exponential of this operator includes a multicontrolled rotation gate. If C were purely real, then the rotation gate would be an $R_X(\theta)=e^{-i\frac{\theta}{2}X}$ gate. If C were purely imaginary, then the rotation gate would be an $R_Y(\theta)=e^{-i\frac{\theta}{2}Y}$ gate. For a complex coefficient, we define

[2]Facing large qubit overheads for second-quantized approaches is not unique to our problem. Different efficient encoding schemes have been developed to tackle this. See, for example [81], or for examples in quantum chemistry see [82,83].

[3]For other quantum algorithms used to carry out time evolution in quantum simulations see e.g. [84,85].

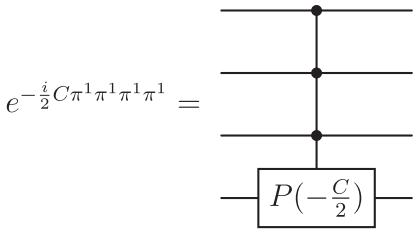


FIG. 7. A quantum gate used for time evolution with the free Hamiltonian. In this four-qubit example, the gate applies $e^{-\frac{i}{2}C}$ only on the computational basis state $|1111\rangle$ and leaves all other fifteen basis states alone. In our delta-pulse simulations, $C(x^+)$ includes either $P^- + Q^-$ or $p^- + q^-$ depending on whether the background field is nonzero at time x^+.

$$R(a,b) = e^{-\frac{i}{2}(aX+bY)} = R_Z(\text{atan2}(b,a))R_X\left(\sqrt{a^2+b^2}\right)R_Z(-\text{atan2}(b,a))\right) \tag{49}$$

where $R_Z(\theta) = e^{-i\frac{\theta}{2}Z}$. The controlled versions of these rotation operators are shown in Fig. 8. However, the matrix exponentials of these Hamiltonian operators are actually Givens rotations [76] shown in Fig. 9. Givens rotation gates rotate two different computational basis states among each other, leaving all other computational basis states alone. They are effectively generalizations of the single-qubit R_X and R_Y gates.

Finally, in the counterterm Hamiltonian, there are $C|\gamma\rangle\langle\gamma|$ and $C|\gamma\rangle\langle\gamma'| + C|\gamma'\rangle\langle\gamma|$ operators with real coefficients (see Sec. III A 1). Matrix exponentials of the former give single-qubit phase gates. Matrix exponentials of the latter lead to a two-qubit Givens rotation gates.

Current quantum hardware do not support multicontrolled CNOT's or phase gates. There exist methods [86] to decompose them into controlled-NOT (CNOT) and T gates that scale linearly in the number of control qubits. Moreover, using ancillae has shown to have significant discounts in these decompositions. Thus, the quantum resources necessary in our quantum simulations predominantly depend on the number N_e of electron-positron pairs. Per time step, there are N_e multicontrolled phase gates, $2N_e$ Givens rotations, and the handful of gates from the counter Hamiltonian. For each gate, the number of control qubits is essentially $k_{e^-e^+}$. If N_t is the number of time steps, then the circuit depth and wall time scale with $k_{e^-e^+}N_eN_t$. If $N_e \approx \binom{n_{e^-e^+}}{k_{e^-e^+}}$, then we conclude that the quantum resources scale polynomially in the number of qubits.

In quantum simulations, we are limited by the number of measurements, or shots, we can perform on a quantum circuit. Rare processes like the helicity flip could require tens of millions of measurements per circuit with physical parameters. To bring the cost down, we scale up the coupling to $e = 2$, which increases the probabilities by a factor of about 10^3. Figure 10 shows a noiseless quantum simulation performed with $(K, N) = (3, 2)$ and $T = 1$. A total of 200 intermediate electron-positron pair states were included in the simulation. With $n_{e^-e^+} = 10$ and choosing $k_{e^-e^+} = 4$, we performed a 12-qubit simulation.

The resource costs for a single Trotter-step circuit, $e^{-\frac{i}{2}H(x_k^+)\Delta x^+}$, were as follows. Before transpilation into purely single- and two-qubit gates, the circuit depth was about 3500 gates, of which about 1000 were expressed as multicontrolled unitaries. After a pass through the QISKIT transpiler [87] (without ancillae), the depth is of the order of 60,000 gates, of which about 26,000 were two-qubit (CNOT) gates and 14,500 were T gates. If two ancilla qubits are allowed and transpilation is done using QISKIT's implementation of the v-chain algorithm [88] to decompose the multicontrolled unitary gates, the circuit depth can be brought down to about 23,500 gates, with about 11,000 CNOT and 5000 T gates.

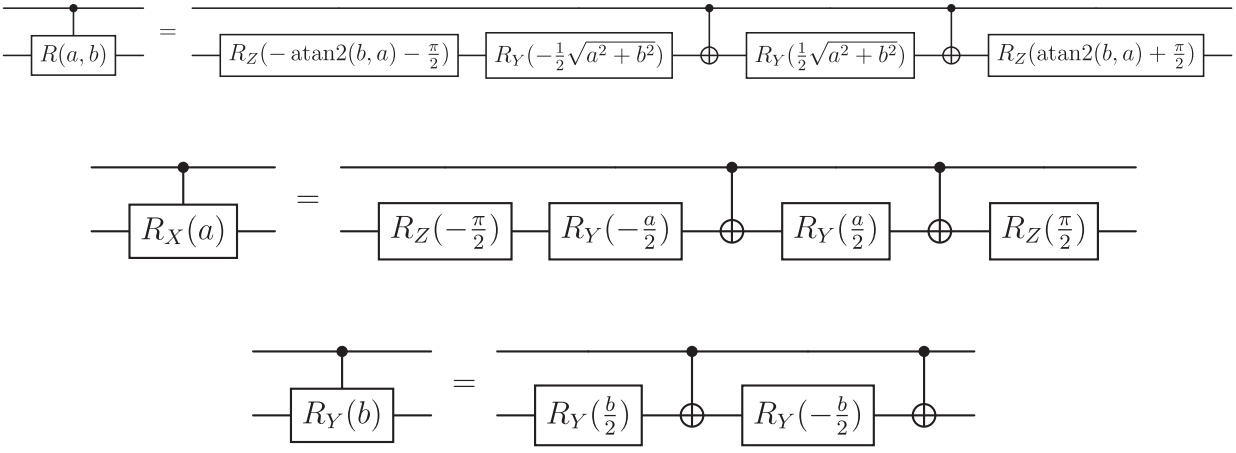


FIG. 8. Controlled rotations when the rotation angles are complex $(a + ib)$, real, or imaginary. These decompositions are useful when quantum hardware does not have native support for controlled unitaries. These gates can be extended to multicontrolled gates by using multicontrolled CNOT's.

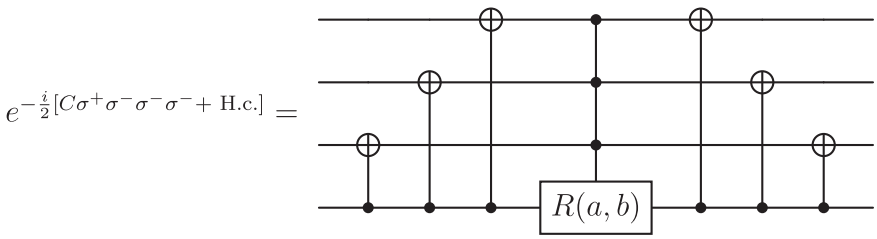


FIG. 9. Givens rotation circuit that performs a portion of the time evolution with the interaction Hamiltonian. The CNOT's diagonalize the string of ladder operators shown in the exponential. They entangle the qubit to be rotated with the rest of the qubits. Note that $C = a + ib$, and in our quantum simulations, C is a coefficient found in the interaction Hamiltonian (5).

For completeness, we estimate the quantum resources needed to implement a single Trotter-step circuit in a simulation utilizing the Jordan-Wigner (JW) transformation. Although two qubits are still needed for the photons, the electrons and positrons each need 200 qubits to encode all helicity and momentum modes used in our discretization. Therefore, a total of 402 qubits would have been required, if we had gone the JW route—this cost is the main reason we opted for the n-choose-k encoding. With the JW transformation, time evolution generated by the free Hamiltonian can be implemented with a total of 400 (single-qubit) phase gates. The time evolution generated by the interaction Hamiltonian would require 400 Givens rotations (200 momentum-conserving electron-positron pairs interacting with two photons) acting on three qubits. Each Givens rotation can be nominally decomposed into four CNOT's and six rotation gates, assuming all-to-all connectivity. However, each Givens rotation comes attached with a product of controlled-Z (CZ) gates that account for fermionic statistics. The exact number depends on the ordering of the Fock basis; for example, we could take the ordering in (39). We estimate of order ∼20 CZ gates per Givens rotation. Time evolution from the counterterm Hamiltonian once again costs two phase gates and two two-qubit Givens rotations acting on the photon qubits. The total cost is roughly 3000 single-qubit gates and 10,000 two-qubit gates, with the dominant cost likely coming from the CZ's of the JW transformation. Note that, in this case, the single- and two-qubit gate decomposition does not include T gates, prior to the synthesis of rotation and phase gates.

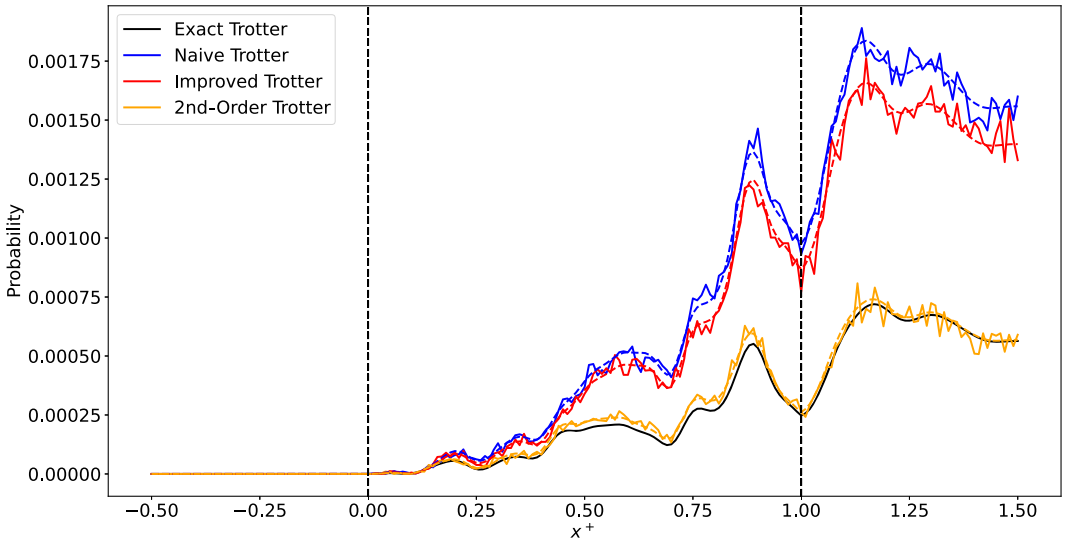


FIG. 10. The importance of second-order Trotterization. The figure above shows the time-dependent polarization flip probabilities obtained from (noiseless) quantum and classical simulations. Here $\Delta x^+ = 0.01$ and $T = 1$. The coupling was increased to $e = 2$ to raise the probabilities and lower the shot requirements. 5×10^5 shots were used for measurements. The dashed vertical lines show when the first and second pulses occur, as well as the moments when adiabatic turn-on ends and adiabatic turn-off begins. The squared S-matrix element (probability) is taken to be the final data point of each curve, once adiabatic turn-off is complete. "Exact Trotter" shows probabilities classically computed with (36). "Naive Trotter" and "Improved Trotter" show two implementations of (48) as explained in the text. "2nd-Order Trotter" shows the implementation of (50). The dashed curves show what the quantum probabilities would be without shot noise. We see that second-order Trotterization is needed for this Δx^+ in order to converge to the result of exact Hamiltonian exponentiation.

The quantum simulation used $\Delta x^+ = 0.01$ for a total of $N_t = 200$ time steps. We find that using (48) leads to significant Trotter error at late times. Moreover, changing the ordering of the decomposition of $H(x_k^+)$ into h operators can modify the Trotter error. In Fig. 10, we demonstrate this phenomenon by using a "naive" decomposition of $H(x_k^+)$ as well as a better motivated "improved" decomposition. The naive decomposition Gray code [76] orders the Givens rotation gates involved in the interaction Hamiltonian evolution according to the relative CNOT's between them. (This would permit a generally greater chance of CNOT cancellations than without the ordering.) With the improved decomposition, we recognize that some elements of H^2 may vanish by a sum of a equal and opposite momenta. Once Trotterized, a product such as $h_i h_j$ may substantially lose this structure. To mitigate this, we order our h operators in the improved decomposition such that subsequent h operators have equal and opposite momenta as much as possible.

Nevertheless, the first-order Trotter error is severe. One option is to use a smaller time step; for example, $\Delta x^+ \to 0.001$. However, this could be too costly. For this reason, we implemented the second-order [89] version of (48):

$$e^{-\frac{i}{2}H(x_k^+)\Delta x^+} = \prod_{h=h_1\cdots h_N} e^{-\frac{i}{4}h\Delta x^+} \prod_{h=h_N\cdots h_1} e^{-\frac{i}{4}h\Delta x^+} + \mathcal{O}[(\Delta x^+)^3]. \tag{50}$$

This second-order Trotterization—along with the aforementioned improved decomposition—dramatically reduces the Trotter error, even agreeing with the "exact" Trotterization within shot noise. In terms of quantum resources, the second-order product formula adds a factor of two to our estimates above.

VI. CONCLUSION

In this paper we have investigated the analytical and computational resources required to perform a Hamiltonian simulation of a one-loop SFQED process. The light-front Hamiltonian was used to perform an adiabatic time evolution of an asymptotic photon Fock state. The main results of our work can be summarized as follows:

(i) Simulating loop-level processes requires confronting symmetry-violating terms stemming from hard momentum cutoffs which are natural and necessary in numerics. We derived counterterms that cancel these spurious effects across a large class of background fields and implemented them in the simulations.

(ii) Devising efficient simulations at loop level requires determining rough boundaries of the space of "relevant" intermediate states for the process of interest, so that the truncation and map to the Hilbert space of the quantum computer reflects these boundaries. In this work we used perturbative formulas to characterize the relevant subspace of intermediate states for given background-field strengths.

(iii) Efficient simulation also requires some optimization of both the qubit encoding and the map from the continuum time evolution operator to quantum gates. We introduced a new n-choose-k encoding to balance qubit count with gate depth and implemented a time evolution circuit based on multicontrolled rotations which allow for a range of optimizations.

(iv) We executed noiseless quantum simulations in order to benchmark truncation and discretization effects and estimate quantum resources required for a full simulation. The number of qubits required for our simulations is practical for near-term quantum devices. However, our circuits are too deep for current quantum computers, and improved gate fidelities and error correction are needed to perform real quantum simulations.

We close by commenting on some directions for future work.

First, while we were able to find appropriate counterterms for our simulations, it would be valuable to have more systematic methods to compute the relevant counterterms for higher-order SFQED processes. Ideally such methods would rely less on perturbation theory than we have, especially if the goal is to simulate nonperturbative phenomena or to tackle regimes of extremely high intensity where the Furry expansion is conjectured to break down [90–92].

Other complications with renormalization can arise with sufficiently aggressive truncations of Fock space, which eliminates some radiative corrections at a given order while retaining others [93] (see [94] for a review of the issues and resolutions.) Fortunately, these complications did not arise for one-loop vacuum polarization in the light front. However, we also note that quantum simulations based on occupation number registers—independent registers of qubits encoding occupation numbers for each single-particle Fock state—probably avoid these issues in a practical sense: to high loop order, no spurious diagram elimination arises.

Quantum computers may one day aid in computing observables in complex systems such as cascades [95–100]. Quantum simulation of these processes would require many more qubits, stemming from the high dimensionality of the multiparticle Hilbert space that the processes explore. It would be interesting to assess the quantum resources needed for an accurate cascade simulation. In particular, it would be useful to compare different qubit encodings for such processes, investigating, for example, the feasibility of Jordan-Wigner versus other encodings.

Relatedly, a comparison of the challenges facing the momentum-space approach with those found in position-space lattice formulations [57,101,102] should be carried out. Rapid progress is being made on simulating spatial lattice gauge theories on quantum computers [14–24,24,103–107], and SFQED should also be studied in this framework. Which approach will be most viable for future quantum hardware remains to be seen.

ACKNOWLEDGMENTS

A. I. thanks Ben King for useful discussions. This work was supported by the U.S. Department of Energy, Office of Science, Office of High Energy Physics Quantum Information Science Enabled Discovery (QuantISED) program. A. I. is supported by the STFC consolidated grant "Particle Theory at the Higgs Centre" ST/X000494/1. This work used the Delta system at the National Center for Supercomputing Applications through allocation PHY230137 from the Advanced Cyberinfrastructure Coordination Ecosystem: Services & Support (ACCESS) program, which is supported by National Science Foundation Grants No. 2138259, No. 2138286, No. 2138307, No. 2137603, and No. 2138296.

DATA AVAILABILITY

The data that support the findings of this article are not publicly available upon publication because it is not technically feasible and/or the cost of preparing, depositing, and hosting the data would be prohibitive within the terms of this research project. The data are available from the authors upon reasonable request.

APPENDIX: HAMILTONIAN FIELD THEORY

This appendix demonstrates how some operators, if generated by cutoff effects in an otherwise well-behaved Hamiltonian, can spoil the symmetry structure and must be canceled by counterterms.

In the text, we calculate amplitudes that only involve photon operators (see Sec. III). Therefore we focus on how the hard momentum cutoffs affect the free Maxwell theory in the light front. Because the cutoffs are not Lorentz covariant, we expect them to generate Lorentz-violating effective operators. We will see that the operators also violate gauge symmetry.

Recall the Maxwell Lagrangian density

$$\mathcal{L} = -\frac{1}{4} F_{\mu\nu} F^{\mu\nu}, \tag{A1}$$

with canonical momentum

$$\Pi^{\mu} = \frac{\partial \mathcal{L}}{\partial(\partial_+ A_\mu)} = F^{\mu +}. \tag{A2}$$

The Hamiltonian is

$$\begin{aligned} H &= \frac{1}{2}\int d^3\mathsf{x}(\Pi^\mu \partial_+ A_\mu - \mathcal{L}) \\ &= \frac{1}{4}\int d^3\mathsf{x}\left(\frac{1}{4}(\Pi^-)^2 + F_{12}^2 - A^-(\partial_- \Pi^- + \partial_i \Pi^i)\right). \end{aligned} \tag{A3}$$

We proceed with canonical quantization, imposing the commutation relations

$$\begin{aligned} [A_\mu(\mathsf{x}), \Pi^\nu(\mathsf{y})] &= i\delta_\mu^\nu \delta^3(\mathsf{x}-\mathsf{y}) \quad [A^\mu(\mathsf{x}), A^\nu(\mathsf{y})] \\ &= 0 = [\Pi^\mu(\mathsf{x}), \Pi^\nu(\mathsf{y})]. \end{aligned} \tag{A4}$$

Our quantized theory has primary constraint $\Pi^+ = 0$. The secondary constraint is

$$[H, \Pi^+] = 0 \Longrightarrow \partial_- \Pi^- + \partial_i \Pi^i \equiv G = 0 \tag{A5}$$

which is Gauss's law. There are no further constraints, because $[H, G] = 0$ and $[\Pi^+, G] = 0$.

1. Counterterms

A covariant regulator would only generate Lorentz- and gauge-invariant effective operators such as F^{2n}. Such operators give correspond to higher-derivative interactions in the Maxwell Hamiltonian. Although our amplitudes contain contributions from these operators, they do not account for the "unphysical contributions" found in Sec. III. Instead, we examine the low-dimension effective operators not of the standard form; namely, the AA and $AA\mathcal{A}\mathcal{A}$ operators found in the text.

Suppose we have an effective Hamiltonian of the form

$$\begin{aligned} H = \frac{1}{4}\int d^3\mathsf{x}\Big(&\frac{1}{4}(\Pi^-)^2 + F_{12}^2 - A^-(\partial_-\Pi^- + \partial_i\Pi^i) \\ &+ C_{AA} A_\mu A^\mu + C_{AA\mathcal{A}\mathcal{A}}(A_\mu A^\mu)(\mathcal{A}_\nu \mathcal{A}^\nu) \\ &+ C_{2A\mathcal{A}}(A_\mu \mathcal{A}^\mu)^2 + D_{\mu\nu\rho\sigma} A^\mu A^\nu \mathcal{A}^\rho \mathcal{A}^\sigma\Big) \end{aligned} \tag{A6}$$

where $D_{\mu\nu\rho\sigma}$ is symmetric and purely off-diagonal in the μ, ν indices and likewise in the ρ, σ indices. Furthermore, $(+,-)$ indices do not mix with (1,2) indices. The secondary constraint from demanding $[H, \Pi^+] = 0$ is now

$$\begin{aligned} &\partial_-\Pi^- + \partial_i\Pi^i - C_{AA}A^+ - C_{AA\mathcal{A}\mathcal{A}}\mathcal{A}_\mu \mathcal{A}^\mu A^+ \\ &\quad - C_{2A\mathcal{A}} A_\mu \mathcal{A}^\mu \mathcal{A}^+ - 2D_{+-\rho\sigma} A^+ \mathcal{A}^\rho \mathcal{A}^\sigma \equiv G = 0. \end{aligned} \tag{A7}$$

However, G does not commute with H:

$$
\begin{aligned}
-2i[H,G] = {} & C_{AA}\left(2\partial_- A^- + \partial_i A^i + \frac{1}{4}\Pi^-\right) \\
& + C_{AA\mathcal{A}\mathcal{A}}\left(\partial_-(\mathcal{A}_\mu \mathcal{A}^\mu A^-) + \partial_i(\mathcal{A}_\mu \mathcal{A}^\mu A^i) + \frac{1}{4}\mathcal{A}_\mu \mathcal{A}^\mu \Pi^- + \mathcal{A}_\mu \mathcal{A}^\mu \partial_- A^-\right) \\
& + C_{2A\mathcal{A}}\left(\partial_-(A_\mu \mathcal{A}^\mu \mathcal{A}^-) + \partial_i(A_\mu \mathcal{A}^\mu \mathcal{A}^i) + \frac{1}{8}\mathcal{A}^+\mathcal{A}^-\Pi^- + \frac{1}{2}\mathcal{A}^+\mathcal{A}^-\partial_- A^- + \frac{1}{2}\mathcal{A}^+\mathcal{A}^-\partial_i A^-\right) \\
& + 2D_{+-\rho\sigma}\partial_-(A^-\mathcal{A}^\rho\mathcal{A}^\sigma) - D_{ij\rho\sigma}\partial_i(A^j\mathcal{A}^\rho\mathcal{A}^\sigma) - D_{+-\rho\sigma}\Pi^-\mathcal{A}^\rho\mathcal{A}^\sigma - 2D_{+-\rho\sigma}\partial_- A^-\mathcal{A}^\rho\mathcal{A}^\sigma. \qquad \text{(A8)}
\end{aligned}
$$

Even in the light-front gauge, this commutator does not vanish. This introduces more constraints; however, each constraint removes a degree of freedom of the photon field. $\Pi^+ = 0$ and $G = 0$ leave the ordinary Maxwell theory with two photon polarizations. In the effective theory, this is no longer the case. Therefore, the effective operators do not preserve the gauge structure of the theory. To fix this, we adjust counterterms for the effective operators, matching the coefficients to the relevant parts of the amplitudes (see Sec. III A 1) in order to cancel off the gauge-violating effects of the momentum cutoffs.

2. Spacetime symmetry breaking

Let K_1, K_2, K_3 and J_1, J_2, J_3 be generators of Lorentz boosts and rotations, respectively. Then generators of the Lorentz group can be defined as [64]

$$
\begin{aligned}
S_1 &= \frac{K_1 - J_2}{\sqrt{2}} \qquad S_2 = \frac{K_2 + J_1}{\sqrt{2}} \qquad K_3, \\
B_1 &= \frac{K_1 + J_2}{\sqrt{2}} \qquad B_2 = \frac{K_2 - J_1}{\sqrt{2}} \qquad J_3. \qquad \text{(A9)}
\end{aligned}
$$

The Maxwell Hamiltonian obeys the following commutation relations:

$$
\begin{aligned}
[K_3, H] &= iH \qquad [S_k, H] = 0 \\
[B_k, H] &= -iP^k \qquad [J_3, H] = 0 \qquad \text{(A10)}
\end{aligned}
$$

where P^k is the generator of (transverse) translations. After fixing the light-front gauge, $A^+ = 0 = \mathcal{A}^+$, as well as using Gauss's law, $\partial_-^2 A^- + \partial_- \partial_i A^i = 0$, the effective operators contain operators of the form

$$
\begin{aligned}
X &\equiv \int d^3\mathbf{x}\, A^1 A^2 + A^2 A^1 \quad \text{(flip)}, \\
O &\equiv \int d^3\mathbf{x}\, A^1 A^1 + A^2 A^2 \quad \text{(no flip)}. \qquad \text{(A11)}
\end{aligned}
$$

We will now check whether these operators respect (A10); if they do not, then they break spacetime symmetries.

a. K_3 transformations

From the equations of motion, $\partial_\mu F^{\mu i} = 0$, we have

$$
4\partial_-\partial_+ A_i = \partial_i \partial_- A^- + \partial_j F_{ji} \Longrightarrow \partial_+ A_i = \frac{1}{4}\partial_\perp^2 \Lambda_i \qquad \text{(A12)}
$$

where Λ_i satisfies $\partial_- \Lambda_i = A_i$. Then when integrating by parts,

$$
\begin{aligned}
\partial_+ X &= \frac{1}{4}\int d^3\mathbf{x}\Big(\partial_-(\Lambda_1 \partial_\perp^2 \Lambda_2) + \partial_-(\Lambda_2 \partial_\perp^2 \Lambda_1)\Big) = 0, \\
\partial_+ O &= \frac{1}{4}\int d^3\mathbf{x}\Big(\partial_-(\Lambda_i \partial_\perp^2 \Lambda_i)\Big) = 0. \qquad \text{(A13)}
\end{aligned}
$$

Therefore, X and O are conserved.

Now using

$$
i[K_3, A^i] = (x^-\partial_- - x^+\partial_+)A^i \qquad \text{(A14)}
$$

we find that

$$
\begin{aligned}
i[K_3, X] &= -X + \int d^3\mathbf{x}\Big(\partial_-(x^- A^1 A^2 + x^- A^2 A^1) - x^+\partial_+(A^1 A^2 + A^2 A^1)\Big) = -X, \\
i[K_3, O] &= -O + \int d^3\mathbf{x}\Big(\partial_-(x^- A^1 A^1 + x^- A^2 A^2) - x^+\partial_+(A^1 A^1 + A^2 A^2)\Big) = -O \qquad \text{(A15)}
\end{aligned}
$$

by boundary conditions.

b. S_k transformations

Using

$$\begin{aligned} -i[S_k, A^i] &= (x^k\partial_+ + x^-\partial_k)A^i - \delta_{ik}A^- + \partial_i\Lambda_k \\ &= (x^k\partial_+ + x^-\partial_k)A^i - \delta_{ik}\partial_j\Lambda_j + \partial_i\Lambda_k \end{aligned} \tag{A16}$$

we find that

$$\begin{aligned} -i[S_k, X] &= \int d^3\mathbf{x}\Big(x^k\partial_+(A^1A^2 + A^2A^1) + x^-\partial_k(A^1A^2 + A^2A^1) \\ &\quad + \delta_{1k}(\partial_i\Lambda_i\partial_-\Lambda_2 + \partial_-\Lambda_2\partial_i\Lambda_i) + \delta_{2k}(\partial_i\Lambda_i\partial_-\Lambda_1 + \partial_-\Lambda_1\partial_i\Lambda_i) \\ &\quad - \partial_1\Lambda_k\partial_-\Lambda_2 - \partial_2\Lambda_k\partial_-\Lambda_1 - \partial_-\Lambda_1\partial_2\Lambda_k - \partial_-\Lambda_2\partial_1\Lambda_k\Big) \\ &= \int d^3\mathbf{x}\Big(x^k\partial_+(A^1A^2 + A^2A^1) + f(\partial\Lambda)\Big), \\ -i[S_k, O] &= \int d^3\mathbf{x}\Big(x^k\partial_+(A^1A^1 + A^2A^2) + x^-\partial_k(A^1A^1 + A^2A^2) \\ &\quad + \delta_{1k}(\partial_i\Lambda_i\partial_-\Lambda_1 + \partial_-\Lambda_1\partial_i\Lambda_i) + \delta_{2k}(\partial_i\Lambda_i\partial_-\Lambda_2 + \partial_-\Lambda_2\partial_i\Lambda_i) - \partial_i\Lambda_i\partial_-\Lambda_k - \partial_-\Lambda_k\partial_i\Lambda_i\Big) \\ &= \int d^3\mathbf{x}\Big(x^k\partial_+(A^1A^1 + A^2A^2)\Big) \end{aligned} \tag{A17}$$

by boundary conditions. The x^k in the integrand prohibits the light-front time derivatives from vanishing.

c. B_k transformations

Using

$$i[B_k, A^i] = (x^+\partial_k + x^k\partial_-)A^i \tag{A18}$$

we find that

$$\begin{aligned} i[B_k, X] &= \int d^3\mathbf{x}\Big(x^+\partial_k(A^1A^2 + A^2A^1) + x^k\partial_-(A^1A^2 + A^2A^1)\Big) = 0, \\ i[B_k, O] &= \int d^3\mathbf{x}\Big(x^+\partial_k(A^1A^1 + A^2A^2) + x^k\partial_-(A^1A^1 + A^2A^2)\Big) = 0 \end{aligned} \tag{A19}$$

by boundary conditions.

d. J_3 transformations

Using

$$i[J_3, A^i] = (x^2\partial_1 - x^1\partial_2)A^i - \epsilon_{ij}A^j \tag{A20}$$

we find that

$$\begin{aligned} i[J_3, X] &= \int d^3\mathbf{x}\Big(x^2\partial_1(A^1A^2 + A^2A^1) - x^1\partial_2(A^1A^2 + A^2A^1) - \epsilon_{1i}(A^iA^2 + A^2A^i) - \epsilon_{2i}(A^iA^1 + A^1A^i)\Big) \\ &= 2\int d^3\mathbf{x}\, A^1A^1 - A^2A^2, \\ i[J_3, O] &= \int d^3\mathbf{x}\Big(x^2\partial_1(A^1A^1 + A^2A^2) - x^1\partial_2(A^1A^1 + A^2A^2) - \epsilon_{1i}(A^iA^1 + A^1A^i) - \epsilon_{2i}(A^iA^2 + A^2A^i)\Big) \\ &= 0 \end{aligned} \tag{A21}$$

by boundary conditions.

e. Verdict

We have found that X-type and O-type operators obey the same commutation relations with K_3 as the Maxwell Hamiltonian does. However, they do not commute with S_k. Therefore, they break transverse spacetime symmetries. X and O commute with B_k, which means they do not contribute to the photon momentum operators. Lastly, X does not commute with J_3 and thus additionally breaks rotational symmetry. Thus the effective operators that contribute to polarization flip amplitudes break spacetime symmetries that should be preserved, and we again conclude that they represent unphysical effects of the cutoff.

[1] J. Schwinger, On gauge invariance and vacuum polarization, Phys. Rev. **82**, 664 (1951).
[2] J. S. Toll, The dispersion relation for light and its application to problems involving electron pairs, Ph.D. thesis, 1952.
[3] N. B. Narozhny, Propagation of plane electromagnetic waves in a constant field, Sov. Phys. JETP **28**, 371 (1969).
[4] T. Heinzl, B. Liesfeld, K.-U. Amthor, H. Schwoerer, R. Sauerbrey, and A. Wipf, On the observation of vacuum birefringence, Opt. Commun. **267**, 318 (2006).
[5] B. King, A. Di Piazza, and C. H. Keitel, A matterless double slit, Nat. Photonics **4**, 92 (2010).
[6] J. M. Cole *et al.*, Experimental evidence of radiation reaction in the collision of a high-intensity laser pulse with a laser-wakefield accelerated electron beam, Phys. Rev. X **8**, 011020 (2018).
[7] K. Poder *et al.*, Experimental signatures of the quantum nature of radiation reaction in the field of an ultraintense laser, Phys. Rev. X **8**, 031004 (2018).
[8] E. E. Los *et al.*, Observation of quantum effects on radiation reaction in strong fields, arXiv:2407.12071.
[9] G. Sarri *et al.*, Input to the european strategy for particle physics: Strong-field quantum electrodynamics, arXiv:2504.02608.
[10] A. Gonoskov, T. G. Blackburn, M. Marklund, and S. S. Bulanov, Charged particle motion and radiation in strong electromagnetic fields, Rev. Mod. Phys. **94**, 045001 (2022).
[11] A. Fedotov, A. Ilderton, F. Karbstein, B. King, D. Seipt, H. Taya, and G. Torgrimsson, Advances in QED with intense background fields, Phys. Rep. **1010**, 1 (2023).
[12] M. T. Hansen, Scattering on periodic lattices, Lect. Notes Phys. **1041**, 43 (2025).
[13] F. Hebenstreit, J. Berges, and D. Gelfand, Simulating fermion production in $1+1$ dimensional QED, Phys. Rev. D **87**, 105006 (2013).
[14] E. Gaz, P. P. Popov, G. Pardo, M. Lewenstein, P. Hauke, and E. Zohar, Quantum simulation of non-Abelian lattice gauge theories: A variational approach to $\mathbb{D}_8$ with dynamical matter, Phys. Rev. Res. **7**, 033012 (2025).
[15] Z. Davoudi, C.-C. Hsieh, and S. V. Kadam, Quantum computation of hadron scattering in a lattice gauge theory, arXiv:2505.20408.
[16] H. Lamm, S. Lawrence, and Y. Yamauchi (NuQS Collaboration), General methods for digital quantum simulation of gauge theories, Phys. Rev. D **100**, 034518 (2019).
[17] A. H. Z. Kavaki and R. Lewis, False vacuum decay in triamond lattice gauge theory, Phys. Rev. D **112**, 014502 (2025).
[18] R. C. Farrell, M. Illa, A. N. Ciavarella, and M. J. Savage, Quantum simulations of hadron dynamics in the Schwinger model using 112 qubits, Phys. Rev. D **109**, 114510 (2024).
[19] E. J. Gustafson, Y. Ji, H. Lamm, E. M. Murairi, S. O. Perez, and S. Zhu, Primitive quantum gates for an $SU(3)$ discrete subgroup: $\Sigma(36\times 3)$, Phys. Rev. D **110**, 034515 (2024).
[20] A. N. Ciavarella, I. M. Burbano, and C. W. Bauer, Efficient truncations of SU(n_c) lattice gauge theory for quantum simulation, arXiv:2503.11888.
[21] S. V. Kadam, A. Naskar, I. Raychowdhury, and J. R. Stryker, Loop-string-hadron approach to SU(3) lattice Yang-Mills theory: Hilbert space of a trivalent vertex, Phys. Rev. D **111**, 074516 (2025).
[22] A. Ciavarella, N. Klco, and M. J. Savage, Trailhead for quantum simulation of SU(3) Yang-Mills lattice gauge theory in the local multiplet basis, Phys. Rev. D **103**, 094501 (2021).
[23] P. Balaji, C. Conefrey-Shinozaki, P. Draper, J. K. Elhaderi, D. Gupta, L. Hidalgo, A. Lytle, and E. Rinaldi, Quantum circuits for SU(3) lattice gauge theory, arXiv:2503.08866.
[24] J. Jiang, N. Klco, and O. D. Matteo, Non-Abelian dynamics on a cube: Improving quantum compilation through qudit-based simulations, arXiv:2506.10945.
[25] J. Schuhmacher, G.-X. Su, J. J. Osborne, A. Gandon, J. C. Halimeh, and I. Tavernelli, Observation of hadron scattering in a lattice gauge theory on a quantum computer, arXiv:2505.20387.
[26] J. C. Halimeh, N. Mueller, J. Knolle, Z. Papić, and Z. Davoudi, Quantum simulation of out-of-equilibrium dynamics in gauge theories, arXiv:2509.03586.
[27] C. W. Bauer *et al.*, Quantum simulation for high-energy physics, PRX Quantum **4**, 027001 (2023).
[28] A. Di Meglio *et al.*, Quantum computing for high-energy physics: State of the art and challenges, PRX Quantum **5**, 037001 (2024).
[29] Z. Davoudi, TASI/CERN/KITP lecture notes on "Toward quantum computing gauge theories of nature", arXiv:2507.15840.
[30] A. T. Than, Y. Y. Atas, A. Chakraborty, J. Zhang, M. T. Diaz, K. Wen, X. Liu, R. Lewis, A. M. Green, C. A. Muschik *et al.*, The phase diagram of quantum chromodynamics in one dimension on a quantum computer, arXiv:2501.00579.

[31] E. Bashore, S. Moretti, and T. Vitos, A quantum algorithm for the n-gluon MHV scattering amplitude, arXiv:2507.14252.
[32] H. A. Chawdhry and M. Pellen, Quantum algorithms for the simulation of QCD processes in the perturbative regime, arXiv:2412.21177.
[33] H. A. Chawdhry, M. Pellen, and S. Williams, Quantum simulation of scattering amplitudes and interferences in perturbative QCD, arXiv:2507.07194.
[34] L. Hidalgo and P. Draper, Quantum simulations for strong-field QED, Phys. Rev. D **109**, 076004 (2024).
[35] I. Tamm, Relativistic interaction of elementary particles, J. Phys. (USSR) **9**, 449 (1945).
[36] S. M. Dancoff, Nonadiabatic meson theory of nuclear forces, Phys. Rev. **78**, 382 (1950).
[37] J. Ingoldby, M. Spannowsky, T. Sypchenko, and S. Williams, Enhancing quantum field theory simulations on NISQ devices with Hamiltonian truncation, Phys. Rev. D **110**, 096016 (2024).
[38] P. Schmoll, J. Naumann, A. Nietner, J. Eisert, and S. Sotiriadis, Hamiltonian truncation tensor networks for quantum field theories, arXiv:2312.12506.
[39] T. Cohen, K. Farnsworth, R. Houtz, and M. A. Luty, Hamiltonian truncation effective theory, SciPost Phys. **13**, 011 (2022).
[40] X. Zhao, A. Ilderton, P. Maris, and J. P. Vary, Scattering in time-dependent basis light-front quantization, Phys. Rev. D **88**, 065014 (2013).
[41] W. Du and J. P. Vary, Systematic input scheme for many-boson Hamiltonians with applications to the two-dimensional ϕ^4 theory, Phys. Rev. D **111**, 016013 (2025).
[42] M. Kreshchuk, W. M. Kirby, G. Goldstein, H. Beauchemin, and P. J. Love, Quantum simulation of quantum field theory in the light-front formulation, Phys. Rev. A **105**, 032418 (2022).
[43] W. Qian, M. Li, C. A. Salgado, and M. Kreshchuk, Efficient quantum simulation of QCD jets on the light front, Phys. Rev. D **111**, 096001 (2025).
[44] S. Meuren, C. H. Keitel, and A. Di Piazza, Polarization operator for plane-wave background fields, Phys. Rev. D **88**, 013007 (2013).
[45] V. Dinu, T. Heinzl, A. Ilderton, M. Marklund, and G. Torgrimsson, Vacuum refractive indices and helicity flip in strong-field QED, Phys. Rev. D **89**, 125003 (2014).
[46] C. Marmier, N. Seegert, and F. Karbstein, Impact of background field localization on vacuum polarization effects, Phys. Rev. D **111**, 016005 (2025).
[47] F. Karbstein, D. Ullmann, E. A. Mosman, and M. Zepf, Direct accessibility of the fundamental constants governing light-by-light scattering, Phys. Rev. Lett. **129**, 061802 (2022).
[48] B. King, T. Heinzl, and T. G. Blackburn, Strong field vacuum birefringence in plane wave pulses, Eur. Phys. J. C **83**, 901 (2023).
[49] A. J. Macleod and B. King, Fundamental constants from photon-photon scattering in three-beam collisions, Phys. Rev. A **110**, 032216 (2024).
[50] B. Shen, Z. Bu, J. Xu, T. Xu, L. Ji, R. Li, and Z. Xu, Exploring vacuum birefringence based on a 100 pw laser and an x-ray free electron laser beam, Plasma Phys. Controlled Fusion **60**, 044002 (2018).
[51] N. Ahmadiniaz *et al.*, Towards a vacuum birefringence experiment at the Helmholtz International Beamline for Extreme Fields (Letter of Intent of the BIREF@HIBEF Collaboration), High Power Laser Sci. Eng. **13**, e7 (2025).
[52] M. Šmíd *et al.*, The darkfield approach to measuring vacuum birefringence and light-by-light couplings—a proof-of-principle experiment, arXiv:2506.11649.
[53] H. G. Rinderknecht *et al.*, On measuring stimulated photon-photon scattering using multiple ultraintense lasers, arXiv:2503.21856.
[54] S. Villalba-Chávez, S. Meuren, and C. Müller, Minicharged particles search by strong laser pulse-induced vacuum polarization effects, Phys. Lett. B **763**, 445 (2016).
[55] S. Villalba-Chávez and C. Müller, Light dark matter candidates in intense laser pulses I: Paraphotons and fermionic minicharged particles, J. High Energy Phys. 06 (2015) 177.
[56] O. Borysov, B. Heinemann, A. Ilderton, B. King, and A. Potylitsyn, Using the nonlinear Breit-Wheeler process to test nonlinear vacuum birefringence, Phys. Rev. D **106**, 116015 (2022).
[57] J. Kogut and L. Susskind, Hamiltonian formulation of Wilson's lattice gauge theories, Phys. Rev. D **11**, 395 (1975).
[58] D. Mustaki, S. Pinsky, J. Shigemitsu, and K. Wilson, Perturbative renormalization of null plane QED, Phys. Rev. D **43**, 3411 (1991).
[59] S. J. Brodsky, H.-C. Pauli, and S. S. Pinsky, Quantum chromodynamics and other field theories on the light cone, Phys. Rep. **301**, 299 (1998).
[60] A. Harindranath, An introduction to light-front dynamics for pedestrians, arXiv:hep-ph/9612244.
[61] T. Heinzl, Light cone quantization: Foundations and applications, Lect. Notes Phys. **572**, 55 (2001).
[62] T. Maskawa and K. Yamawaki, The problem of $p^+ = 0$ mode in the null-plane field theory and Dirac's method of quantization, Prog. Theor. Phys. **56**, 270 (1976).
[63] T. Heinzl, Light-cone zero modes revisited, arXiv:hep-th/0310165.
[64] J. B. Kogut and D. E. Soper, Quantum electrodynamics in the infinite-momentum frame, Phys. Rev. D **1**, 2901 (1970).
[65] W. H. Furry, On bound states and scattering in positron theory, Phys. Rev. **81**, 115 (1951).
[66] D. M. Wolkow, Uber eine Klasse von Losungen der Diracschen Gleichung, Z. Phys. **94**, 250 (1935).
[67] A. M. Fedotov and A. A. Mironov, Pair creation by collision of an intense laser pulse with a high-frequency photon beam, Phys. Rev. A **88**, 062110 (2013).
[68] A. Ilderton, Exact results for scattering on ultrashort plane wave backgrounds, Phys. Rev. D **100**, 125018 (2019).
[69] A. Ilderton and H. Kingham, Vacuum polarization effects in impulsive fields, Phys. Rev. D **110**, 105022 (2024).
[70] T. G. Blackburn, Theory uncertainties in predictions of strong-field QED, arXiv:2508.03975.
[71] A. Di Piazza, M. Tamburini, S. Meuren, and C. H. Keitel, Implementing nonlinear Compton scattering beyond the

local constant field approximation, Phys. Rev. A **98**, 012134 (2018).
[72] A. Ilderton, B. King, and D. Seipt, Extended locally constant field approximation for nonlinear Compton scattering, Phys. Rev. A **99**, 042121 (2019).
[73] J. Huyghebaert and H. D. Raedt, Product formula methods for time-dependent schrodinger problems, J. Phys. A **23**, 5777 (1990).
[74] B. Hu, A. Ilderton, and X. Zhao, Scattering in strong electromagnetic fields: Transverse size effects in time-dependent basis light-front quantization, Phys. Rev. D **102**, 016017 (2020).
[75] G. Chen, X. Zhao, Y. Li, K. Tuchin, and J. P. Vary, Particle distribution in intense fields in a light-front Hamiltonian approach, Phys. Rev. D **95**, 096012 (2017).
[76] M. A. Nielsen and I. L. Chuang, *Quantum Computation and Quantum Information: 10th Anniversary Edition* (Cambridge University Press, Cambridge, England, 2010).
[77] A. Barenco, C. H. Bennett, R. Cleve, D. P. DiVincenzo, N. Margolus, P. Shor, T. Sleator, J. A. Smolin, and H. Weinfurter, Elementary gates for quantum computation, Phys. Rev. A **52**, 3457 (1995).
[78] R. Somma, G. Ortiz, J. E. Gubernatis, E. Knill, and R. Laflamme, Simulating physical phenomena by quantum networks, Phys. Rev. A **65**, 042323 (2002).
[79] J. T. Seeley, M. J. Richard, and P. J. Love, The Bravyi-Kitaev transformation for quantum computation of electronic structure, J. Chem. Phys. **137**, 224109 (2012).
[80] O. O'Brien and S. Strelchuk, Ultrafast hybrid fermion-to-qubit mapping, Phys. Rev. B **109**, 115149 (2024).
[81] W. M. Kirby, S. Hadi, M. Kreshchuk, and P. J. Love, Quantum simulation of second-quantized Hamiltonians in compact encoding, Phys. Rev. A **104**, 042607 (2021).
[82] Y. Shee, P.-K. Tsai, C.-L. Hong, H.-C. Cheng, and H.-S. Goan, Qubit-efficient encoding scheme for quantum simulations of electronic structure, Phys. Rev. Res. **4**, 023154 (2022).
[83] B. Huang, N. Sheng, M. Govoni, and G. Galli, Quantum simulations of fermionic Hamiltonians with efficient encoding and ansatz schemes, J. Chem. Theory Comput. **19**, 1487 (2023).
[84] S. Hariprakash, N. S. Modi, M. Kreshchuk, C. F. Kane, and C. W. Bauer, Strategies for simulating the time evolution of Hamiltonian lattice field theories, Phys. Rev. A **111**, 022419 (2025).
[85] J. M. Martyn, Z. M. Rossi, A. K. Tan, and I. L. Chuang, Grand unification of quantum algorithms, PRX Quantum **2**, 040203 (2021).
[86] B. Zindorf and S. Bose, Efficient implementation of multi-controlled quantum gates, arXiv:2404.02279.
[87] A. Javadi-Abhari, M. Treinish, K. Krsulich, C. J. Wood, J. Lishman, J. Gacon, S. Martiel, P. D. Nation, L. S. Bishop, A. W. Cross *et al.*, Quantum computing with Qiskit, arXiv:2405.08810.
[88] A. Bennakhi, P. Franzon, and G. T. Byrd, Analyzing quantum circuit depth reduction with ancilla qubits in MCX gates, arXiv:2408.01304.
[89] T. N. Ikeda, A. Abrar, I. L. Chuang, and S. Sugiura, Minimum trotterization formulas for a time-dependent Hamiltonian, Quantum **7**, 1168 (2023).
[90] V. I. Ritus, Radiative effects and their enhancement in an intense electromagnetic field, Sov. Phys. JETP **30**, 1181 (1970).
[91] N. B. Narozhnyi, Expansion parameter of perturbation theory in intense field quantum electrodynamics, Phys. Rev. D **21**, 1176 (1980).
[92] A. Fedotov, Conjecture of perturbative QED breakdown $\alpha\chi^{2/3} \gtrsim 1$, J. Phys. Conf. Ser. **826**, 012027 (2017).
[93] R. J. Perry, A. Harindranath, and K. G. Wilson, Light front Tamm-Dancoff field theory, Phys. Rev. Lett. **65**, 2959 (1990).
[94] J. R. Hiller, Nonperturbative light-front Hamiltonian methods, Prog. Part. Nucl. Phys. **90**, 75 (2016).
[95] A. R. Bell and J. G. Kirk, Possibility of prolific pair production with high-power lasers, Phys. Rev. Lett. **101**, 200403 (2008).
[96] N. V. Elkina, A. M. Fedotov, I. Y. Kostyukov, M. V. Legkov, N. B. Narozhny, E. N. Nerush, and H. Ruhl, QED cascades induced by circularly polarized laser fields, Phys. Rev. ST Accel. Beams **14**, 054401 (2011).
[97] A. A. Mironov, E. G. Gelfer, and A. M. Fedotov, Onset of electron-seeded cascades in generic electromagnetic fields, Phys. Rev. A **104**, 012221 (2021).
[98] M. Pouyez, A. A. Mironov, T. Grismayer, A. Mercuri-Baron, F. Perez, M. Vranic, C. Riconda, and M. Grech, Multiplicity of electron- and photon-seeded electromagnetic showers at multipetawatt laser facilities, Phys. Rev. E **110**, 065208 (2024).
[99] A. Mercuri-Baron, A. A. Mironov, C. Riconda, A. Grassi, and M. Grech, Growth rate of self-sustained QED cascades induced by intense lasers, Phys. Rev. X **15**, 011062 (2025).
[100] M. Pouyez, T. Grismayer, M. Grech, and C. Riconda, Kinetic structure of strong-field QED showers in crossed electromagnetic fields, Phys. Rev. Lett. **134**, 135001 (2025).
[101] E. Zohar and M. Burrello, Formulation of lattice gauge theories for quantum simulations, Phys. Rev. D **91**, 054506 (2015).
[102] G. Magnifico, T. Felser, P. Silvi, and S. Montangero, Lattice quantum electrodynamics in $(3+1)$-dimensions at finite density with tensor networks, Nat. Commun. **12**, 3600 (2021).
[103] A. Kan, L. Funcke, S. Kühn, L. Dellantonio, J. Zhang, J. F. Haase, C. A. Muschik, and K. Jansen, Investigating a $(3+1)$D topological θ-term in the Hamiltonian formulation of lattice gauge theories for quantum and classical simulations, Phys. Rev. D **104**, 034504 (2021).
[104] D. M. Grabowska, C. F. Kane, and C. W. Bauer, Fully gauge-fixed SU(2) Hamiltonian for quantum simulations, Phys. Rev. D **111**, 114516 (2025).
[105] Z. Li, D. M. Grabowska, and M. J. Savage, Sequency hierarchy truncation (seqht) for adiabatic state preparation and time evolution in quantum simulations, arXiv:2407.13835.
[106] A. Crippa, K. Jansen, and E. Rinaldi, Analysis of the confinement string in $(2+1)$-dimensional quantum electrodynamics with a trapped-ion quantum computer, arXiv:2411.05628.
[107] E. Gustafson and R. V. de Water, Improved fermion Hamiltonians for quantum simulation, arXiv:2402.04317.